

# Far-field high-energy diffraction microscopy: a tool for intergranular orientation and strain analysis

J V Bernier<sup>1\*</sup>, N R Barton<sup>1</sup>, U Lienert<sup>2</sup>, and M P Miller<sup>3</sup>

<sup>1</sup>Lawrence Livermore National Laboratory, Livermore, California, USA

<sup>2</sup>Argonne National Laboratory, Argonne, Illinois, USA

<sup>3</sup>Cornell University, Ithaca, New York, USA

*The manuscript was received on 16 November 2010 and was accepted after revision for publication on 11 March 2011.*

DOI: 10.1177/0309324711405761

**Abstract:** The far-field high-energy diffraction microscopy technique is presented in the context of high-energy synchrotron x-ray diffraction. For each grain in an illuminated polycrystalline volume, the volume-averaged lattice orientations, lattice strain tensors, and centre-of-mass (COM) coordinates may be determined to a high degree of precision: better than  $0.05^\circ$ ,  $1 \times 10^{-4}$ , and 0.1 pixel, respectively. Because the full lattice strain tensors are available, corresponding mean stress tensors may be calculated unambiguously using single-crystal elastic moduli. A novel formulation for orientation indexing and cell refinement is introduced and demonstrated using two examples: first, sequential indexing and lattice refinement of a single-crystal ruby standard with known COM coordinates; and second, indexing and refinement of simulated diffraction data from an aggregate of 819 individual grains using several sample rotation ranges and including the influence of experimental uncertainties. The speed of acquisition and penetration depth achievable with high-energy (that is,  $>50$  keV) x-rays make this technique ideal for studies of strain/stress evolution in situ, as well as for residual stress analysis.

**Keywords:** HEDM, 3DXRD, polycrystalline materials, strain tensor, stress tensor, synchrotron radiation, x-ray diffraction, computer programs

## 1 INTRODUCTION

An empirical understanding of the most salient structure/mechanical property relationships exists for many alloy systems. Such an understanding, however, generally fails to provide a truly predictive capability for capturing the mechanical response of a polycrystalline aggregate. Both anisotropy in the mechanical properties of single crystals and complex intergranular interactions can lead to significant deformation heterogeneity even under macroscopically simple loading conditions. As a result, the development of crystal-scale models that accurately capture deformation behaviour *within* a polycrystalline aggregate remains a vast research frontier.

Unfortunately, the relative lack of experimental data – particularly three-dimensional – at the relevant length scale has seriously retarded efforts to validate such models. Much has been learned from mechanical tests on large single crystals; certainly an understanding of phenomena such as crystallographic slip under simple loading conditions (for example, uniaxial tension) has been gained. However, single crystals of many alloy systems are extraordinarily difficult, if not impossible, to obtain. Much has also been learned from aggregate-averaged diffraction measurements during in situ deformation [1–3], but the superposed nature of the data limits the ability to isolate the relative effects of specific microstructural features and deformation mechanisms. Therefore probes of the crystal-scale *stress–strain* responses deep within deforming aggregates are vitally needed. As evidenced by many recent publications, high-energy synchrotron x-ray diffraction

\*Corresponding author: Lawrence Livermore National Laboratory, Livermore, CA 94550, USA.  
email: bernier2@llnl.gov

experiments employing in situ loading hold enormous potential as such grain-scale probes of mechanical behaviour [4–9].

Synchrotron light sources have become an indispensable tool in the field of experimental mechanics, as the combination of high flux and high energy have enabled in situ observations of evolving microstructure and micromechanical state in bulk metallic samples. The far-field high-energy diffraction microscopy (HEDM) method presented herein was developed following the work of Poulsen *et al.* [10] and Lauridsen *et al.* [11] on the three-dimensional (3D) x-ray diffraction (3DXRD) method. Far-field HEDM is a transmitted beam, rotating crystal technique that interrogates embedded neighbourhoods of grains simultaneously. This is in contrast to the Laue microdiffraction technique developed by Larson *et al.* [12] and Tamura *et al.* [13] in which a micron-sized polychromatic beam is rastered over the sample surface to generate local maps of lattice orientation and (deviatoric) strain over a sample volume encompassing a small neighbourhood of grains [14–16].

Margulies *et al.* [4] and Martins *et al.* [5] demonstrated the feasibility of applying the 3DXRD technique for obtaining fully 3D lattice strain tensors for individual grains embedded in polycrystalline specimens subject to loading in situ. More recently, Mosciki *et al.* [17] and Oddershede *et al.* [9] have pushed the limits of resolution while extending the technique to encompass large aggregates (~1000 grains). Note that the far-field techniques lack intragranular resolution; the orientations and strain tensors obtained are volumetric averages over the individual grains, a condition that puts some restrictions on the gross shape and extent of the measured diffraction spots. In this paper we present a method for identifying an embedded neighbourhood of grains by orientation indexing, and subsequently determining the centre-of-mass coordinates and mean strain tensor for each grain. The HEDM method presented here differs from the recent work of Oddershede *et al.* [9] in two main aspects:

- (a) the orientation indexing method;
- (b) the use of finite deformation kinematics to represent the distorted unit cell.

We also seek to provide a more rigorous verification and validation of the HEDM methodology using two carefully constructed example applications rather than presenting an application to measured data for which the exact parameters of the grain population are not known. There are various choices for strain measures that can be calculated from the distorted lattice with respect to some *strain-free*

reference lattice. A method for calculating strain measures that is crystallographically self-consistent with the application of symmetry is presented. Stress tensors can in turn be calculated directly from the strain tensors using anisotropic linear elasticity.

In the far-field geometry, the detector distance is large (for example, ~1 m) with respect to the beam dimensions defining the diffraction volume. As such, the positions of the diffracted beams on the detector are dominated by the x-ray energy and the crystal lattice configurations of diffracting grains rather than their positions in the beam; all spots lie approximately on the Debye–Scherrer rings associated with the reference unit cell(s). Nevertheless, the 3D data obtained using a single fixed detector are shown to provide sufficient resolution to determine the centres of mass of equiaxed grains to within ~10  $\mu\text{m}$  (see section 3.1). Near-field analogues to the HEDM method presented in this paper are being developed by Suter *et al.* [18, 19] and Ludwig *et al.* [20], among others. In the near-field geometry, spatial resolution is gained at the expense of angular (read: strain) resolution by employing a working distance on the order of the diffraction volume dimensions (for example, ~1–10 mm). These techniques provide spatial orientation maps, which may be processed to reveal grain boundary networks in 3D [20, 21]. A multi-detector instrument that enables both near- and far-field data acquisition is currently available at beamline ID-11 of the European Synchrotron Radiation Facility (<http://www.esrf.eu>), and two more are under development at the Advanced Photon Source (<http://www.aps.anl.gov>) and Petra-III (<http://petra3.desy.de/>), respectively.

For the most part, the diffraction probes provided by the 3DXRD and HEDM efforts have to date merely demonstrated the utility of the experiments. Instead of acquiring data from a large statistically significant number of grains, the tendency in the early experiments has been to focus more on proof of concept by using strong reflections from a few favourably oriented grains(s). However, transitioning the method from such a *heroic effort* to an actual capability – i.e. to move the exploratory science from the development of the experiment to the understanding of the material response – has been a major undertaking. The development of electron backscatter diffraction (EBSD) via scanning electron microscope (SEM) as the de facto standard microstructure analysis tool is an excellent example of such an evolution. Early EBSD efforts focused on demonstrating that the full lattice orientation could be obtained by analysing the Kikuchi patterns [22]. Indexing more than a handful of Kikuchi patterns, however, was prohibitive until the process was automated through

the work of Wright *et al.* [23]. A great deal of effort was expended beyond the pure discovery phase to turn EBSD into a capability, but now almost every paper published in the area of polycrystalline metals contains an EBSD – or orientation imaging microscopy – orientation map. The HEDM technique is currently at this pivotal developmental moment, and there are several groups working to achieve the methodological and algorithmic breakthroughs that will enable its more widespread application in the field. Several key capabilities have enabled the collection of data from an entire neighbourhood of grains simultaneously during in situ loading. This is in contrast to early 3DXRD experiments where the crystal or grain of interest was manually centred on the goniometer axis to prevent precession and simplify the data reduction [6, 8]. As with automated EBSD, high-speed x-ray detectors have enabled collection of multiple diffraction patterns per second. In addition, new detector control algorithms have enabled literally continuous loading [24].

In the method described herein, entire neighbourhoods of grains are characterized simultaneously using fixed *box* beam and single rotation axis perpendicular to it. This includes centre-of-mass coordinates, orientations, lattice strain tensors. In one of the seminal 3DXRD references, Margulies *et al.* [4] suggested that with enough reflections, complete characterization of many grains should be theoretically possible. In the current paper, we describe a working methodology to achieve precisely that end: determining the orientation, centroid location and lattice strain tensor of multiple grains within a deforming polycrystalline aggregate.

The overall goals of this paper are (i) to detail the data reduction methodology developed for full characterization of the deforming aggregate, (ii) to demonstrate the method using results from a manually offset ruby single-crystal standard, and (iii) to demonstrate an application for studying a polycrystalline sample using simulated diffraction data. This experimental framework is currently being implemented at beamline 1-ID-C at the Advanced Photon Source for determining the centroids, orientations and lattice strain tensors for individual grains embedded within polycrystals during thermo-mechanical processing in situ. We seek to illustrate the immense potential of this experimental capability.

The data reduction methodology is outlined in detail in section 2. The method is exercised in section 3.1 via the determination of orientation, lattice parameters (equivalent to strain determination), and centroidal coordinates of a ruby single crystal (NIST SRM 1990) for six prescribed centroidal displacement vectors. In section 3.2, the ability to

process large aggregates is illustrated using simulated diffraction data from an aggregate of 819 grains with randomly assigned orientations and strain states. We consider results described here as the current state of our experimental capability. We conclude with suggestions for future experiments and areas for improvement in the data reduction methodology. All data and software used in this work can be provided upon request.

## 2 HEDM METHOD

The far-field HEDM method is essentially a rotating-crystal method (see Cullity [25], Warren [26]) using high-energy synchrotron x-rays and an area detector at a large working distance. The fundamental experimental setup – shown schematically in Figure 1(a) – has been described previously in

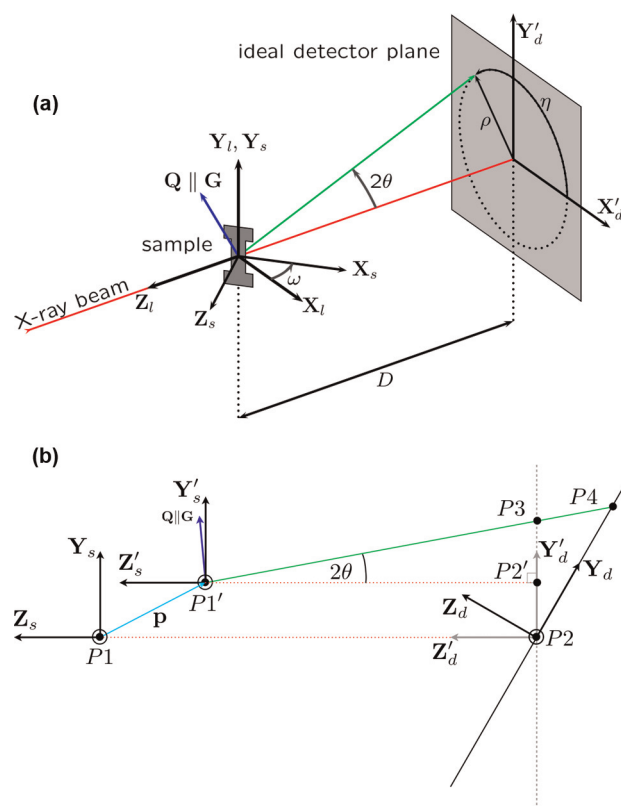


**Fig. 1** Schematic describing the geometry of the far-field HEDM instrument (a), and the detector and sample coordinate systems (b). Note that (a) does not show the geometry of the tilted (actual) detector plane, nor the local coordinate system of grains that are not centered in the x-ray beam for clarity; these coordinate systems,  $\{X'_s, Y'_s, Z'_s\}$  and  $\{X'_d, Y'_d, Z'_d\}$ , are shown in a simplified 2-d plan view ( $\eta = 90^\circ$ ,  $\omega = 0^\circ$ ,  $p_x = 0$ ) in (b)

references [4, 5, 7, 9, 11]. Positioning stages below the rotational stage (along  $\mathbf{X}_i$ ) and above it (along each axis of  $\{\mathbf{X}_s, \mathbf{Y}_s, \mathbf{Z}_s\}$ ) are required to (i) centre the rotation axis onto the x-ray beam, and (ii) centre the sample (or a particular embedded grain) on the rotation axis. High angular resolution is achieved via small effective pixel size at a large working distance, and large volumes of reciprocal space may be interrogated by (i) using a large detector and high-energy x-rays such that multiple orders of diffraction are compressed into the viewing angle  $2\theta$ , and (ii) by rotating the sample through a large range of  $\omega$ .

The primary role of the data reduction is to accurately assign reciprocal lattice vectors to diffraction spots, as described in section 2.2. The components of the reciprocal lattice vectors (or equivalently scattering vectors) are derived from the centres of the diffraction signals, or *spots*. The centres of these spots may be obtained from intensity-weighted centroids in thresholded segmentation algorithms (less accurate), or by fitting them with symmetric profile functions such as elliptical Gaussians (more accurate). The uncertainty in such fit Bragg peak positions has been discussed by Withers *et al.* [27] in the context of 1D peaks obtained via neutron diffraction; a similar study in the context of 3D diffraction signal, synchrotron x-ray diffraction, and flat-panel detectors has been recently undertaken by Edmiston *et al.* [28].

## 2.1 Mathematical conventions

In order to describe the HEDM method in detail, it is necessary to define several coordinate systems. The crystal lattice itself may be parametrized by its primitive vectors  $\mathbf{a}$ ,  $\mathbf{b}$ , and  $\mathbf{c}$ . They share a common origin at a lattice site and are subject to the conditions

$$\begin{aligned} \|\mathbf{a}\| &= a \\ \|\mathbf{b}\| &= b \\ \|\mathbf{c}\| &= c \\ \frac{1}{bc}\mathbf{b} \cdot \mathbf{c} &= \cos \alpha \\ \frac{1}{ca}\mathbf{c} \cdot \mathbf{a} &= \cos \beta \\ \frac{1}{ab}\mathbf{a} \cdot \mathbf{b} &= \cos \gamma \end{aligned} \quad (1)$$

The six scalar cell parameters  $\{a, b, c, \alpha, \beta, \gamma\}$  represent a convenient parametrization of the reference unit cell, which typically correspond to an unloaded state at a reference temperature. Crystal symmetry operations (excluding triclinic) generate equivalences among cell parameters; however once a crystal is deformed, the reference symmetry is broken and all six parameters must be considered as independent. The treatment of strained crystals in the

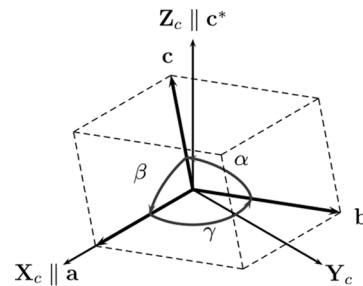


**Fig. 2** The convention for describing the reference (read: unstrained) lattice has  $\mathbf{a} \parallel \mathbf{X}_c$  and  $\mathbf{c}^* \parallel \mathbf{Z}_c$ . Note that a triclinic primitive cell is depicted for generality. The crystal orientation,  $R_c^s$ , takes components in the crystal frame,  $\{\mathbf{X}_c, \mathbf{Y}_c, \mathbf{Z}_c\}$ , to the sample frame,  $\{\mathbf{X}'_s, \mathbf{Y}'_s, \mathbf{Z}'_s\}$

context of the reference crystal symmetry is discussed in detail in section 2.6.

For writing components of crystal-relative vectors and tensors, it is convenient to define a right-handed orthonormal (RHON) frame,  $\{\mathbf{X}_c, \mathbf{Y}_c, \mathbf{Z}_c\}$ , that is fixed to the reference crystal lattice. The convention employed herein is consistent with that proposed by Nye [29]. Explicitly stated,  $\mathbf{a} \parallel \mathbf{X}_c$  and  $(\mathbf{a} \times \mathbf{b}) \parallel \mathbf{Z}_c$ , as depicted in Fig. 2. The change-of-basis matrix,  $A$ , that takes components in the direct lattice to the crystal frame is

$$\begin{aligned} A &= [\mathbf{a} \quad \mathbf{b} \quad \mathbf{c}]_c \\ &= \begin{bmatrix} a & b \cos \gamma & c \cos \beta \\ 0 & b \sin \gamma & -c \sin \beta \cos \alpha^* \\ 0 & 0 & c \sin \beta \sin \alpha^* \end{bmatrix} \end{aligned} \quad (2)$$

where  $\cos \alpha^* = \frac{\cos \beta \cos \gamma - \cos \alpha}{\sin \beta \sin \gamma}$  and  $[\cdot]_c$  denotes components in the crystal frame (see 30).

The reciprocal lattice, which forms a dual basis to the direct lattice, is a very useful concept in diffraction [25, 31] and is used extensively in section 2.2. The reciprocal lattice vectors are defined<sup>†</sup> as

$$\mathbf{a}^* = \frac{1}{v} \mathbf{b} \times \mathbf{c} \quad (3)$$

$$\mathbf{b}^* = \frac{1}{v} \mathbf{c} \times \mathbf{a} \quad (4)$$

$$\mathbf{c}^* = \frac{1}{v} \mathbf{a} \times \mathbf{b} \quad (5)$$

where  $v = \mathbf{a} \cdot \mathbf{b} \times \mathbf{c}$  represents the volume of the primitive cell. The change-of-basis matrix,  $B$ , that takes components in the reciprocal lattice to the crystal frame is written analogously to equation (2) as

<sup>†</sup>This is the so-called crystallographer's convention where the prefactor of  $2\pi$  is omitted.

$$\mathbf{B} = [\mathbf{a}^* \quad \mathbf{b}^* \quad \mathbf{c}^*]_c = \frac{1}{v} \begin{bmatrix} bc \sin \alpha^* \sin \beta \sin \gamma & 0 & 0 \\ -bc \sin \alpha^* \sin \beta \cos \gamma & ac \sin \alpha^* \sin \beta & 0 \\ -bc(\cos \alpha^* \sin \beta \cos \gamma + \cos \beta \sin \gamma) & ac \cos \alpha^* \sin \beta & ab \sin \gamma \end{bmatrix} \quad (6)$$

where  $\{\alpha^*, b^*, c^*, \alpha^*, \beta^*, \gamma^*\}$  are the reciprocal lattice parameters defined analogously to the direct lattice parameters in Fig. 2 and equation (1).

A second RHON frame,  $\{\mathbf{X}_s \mathbf{Y}_s \mathbf{Z}_s\}$ , is attached to the polycrystalline sample (see Fig. 1). Typically the choice of axes is significant with respect to processing history (for example, rolling, transverse, and normal directions for samples cut from rolled sheet) or applied load (for example, tensile axis). This frame also facilitates the definition of the crystal (grain) orientation as the change-of-basis matrix,  $\mathbf{R}_c^s$ , that takes components from  $\{\mathbf{X}_c \mathbf{Y}_c \mathbf{Z}_c\} \rightarrow \{\mathbf{X}_s \mathbf{Y}_s \mathbf{Z}_s\}$ . In the lexicon of Kocks [32], this definition of an orientation is referred to as the *lattice orientation*.

A third RHON frame,  $\{\mathbf{X}_l \mathbf{Y}_l \mathbf{Z}_l\}$ , is fixed with respect to the x-ray beam and oscillation axis of the goniometer (see Fig. 1). The sample and laboratory frames are related to each other by a rotation of  $\omega$  about  $\mathbf{Y}_l$ , and  $\mathbf{Z}_l$  is directed upstream of the incident x-ray beam. The change-of-basis matrix,  $\mathbf{R}_s^l$ , that takes components in  $\{\mathbf{X}_s \mathbf{Y}_s \mathbf{Z}_s\} \rightarrow \{\mathbf{X}_l \mathbf{Y}_l \mathbf{Z}_l\}$  is then

$$\mathbf{R}_s^l = \begin{bmatrix} \cos \omega & 0 & \sin \omega \\ 0 & 1 & 0 \\ -\sin \omega & 0 & \cos \omega \end{bmatrix} \quad (7)$$

A fourth RHON frame,  $\{\mathbf{X}_d \mathbf{Y}_d \mathbf{Z}_d\}$ , is attached to the detector plane and is used to measure the positions of diffracted beams in the experiment (see Fig. 1). The origin is defined as the intersection of the direct beam ( $-\mathbf{Z}_d$ ) and the image plane,  $\mathbf{X}_d$  is aligned with the image horizontal,  $\mathbf{Y}_d$  is aligned with the image vertical, and  $\mathbf{Z}_d$  is the detector plane normal. Note that in general the detector will be slightly tilted such that  $\mathbf{Z}'_d \parallel \mathbf{Z}_l$ .

A fifth RHON frame,  $\{\mathbf{X}'_d \mathbf{Y}'_d \mathbf{Z}'_d\}$ , represents the *ideal* or untilted detector frame. It shares the same origin as  $\{\mathbf{X}_d \mathbf{Y}_d \mathbf{Z}_d\}$ , but  $\mathbf{X}'_d \parallel \mathbf{X}_l$ ,  $\mathbf{Y}'_d \parallel \mathbf{Y}_l$ , and  $\mathbf{Z}'_d \parallel \mathbf{Z}_l$ . This frame is useful for describing the coordinates of a diffracted beam, which is discussed later. The determination of the change-of-basis matrix,  $\mathbf{T}$ , that takes components in  $\{\mathbf{X}_d \mathbf{Y}_d \mathbf{Z}_d\}$  to  $\{\mathbf{X}'_d \mathbf{Y}'_d \mathbf{Z}'_d\}$  is a critical step in the calibration of the diffraction instrument.

Lastly, it is necessary to define a sixth RHON frame,  $\{\mathbf{X}'_s \mathbf{Y}'_s \mathbf{Z}'_s\}$ , in cases where the grain is smaller than the diffraction volume (see Fig. 1(b)). This frame is related to  $\{\mathbf{X}_s \mathbf{Y}_s \mathbf{Z}_s\}$  by a translation vector,  $\mathbf{p}$ , which represents the coordinates of the grain centre-of-mass in the sample frame. In cases where  $\mathbf{p} \neq \mathbf{0}$ , properly relating the values of the

observed angles  $2\theta$  and  $\eta$  to the underlying grain requires an  $\omega$ -dependent correction (that is, the action of  $\mathbf{R}_s^l$  on  $\mathbf{p}$ ). This is due to the fact that  $2\theta$  and  $\eta$  are directly related to reciprocal lattice vectors, which are in turn determined by the position and orientation of the diffracting grain's crystal lattice. These relationships are discussed further in section 2.2. Conversely, systematic (read: harmonic) deviations in measured diffraction spots that have been associated with a grain can be exploited to determine  $\mathbf{p}$ , which is discussed in section 2.6.2.

## 2.2 Diffraction

Reciprocal lattice vectors, denoted as  $\mathbf{G}$ , are perpendicular to the crystallographic planes whose Miller indices are equivalent to their components in the reciprocal lattice [25, 31]. Let  $d_G$  represent the spacing between the crystallographic planes having normals  $\mathbf{n} \parallel \mathbf{G}$ . In the chosen convention,  $d_G = 1/\|\mathbf{G}\|$ . Diffraction is observed when the Bragg condition

$$\lambda = 2d_G \sin \theta_G \quad (8)$$

is satisfied; here  $\lambda$  is the x-ray wavelength and  $\theta_G$  is the scattering angle associated with  $\mathbf{G}$ . The scattering angle is equivalently defined as the grazing angle between the x-ray beam and the diffracting plane, or half the angle between the direct (transmitted) and diffracted beams (see Figs 1(a) and (b)).

Let  $\mathbf{Q}$  denote a scattering vector associated with an observed diffracted beam. For elastic scattering – as is employed by the HEDM method – the Bragg condition can be written equivalently as

$$\mathbf{Q} - \mathbf{G} = \mathbf{0} \quad (9)$$

The three equations in the components of this vector equation are known as the Laue conditions Cullity [25, 31]. Equations (8) and (9) imply that  $\mathbf{Q}$  satisfies

$$\frac{\mathbf{Q}}{\|\mathbf{Q}\|} \cdot \mathbf{Z}_l = \sin \theta \quad (10)$$

Equation (E: bragg Condition Q) describes the locus of scattering vectors that satisfy a specific Bragg condition: a cone aligned with the incident x-ray beam opening upstream from the sample with vertex angle  $\pi - 2\theta$ . The size and position of the detector determines the maximum visible scattering angle,  $2\theta_{\max}$ . For all reciprocal lattice vectors having associated  $2\theta_G < 2\theta_{\max}$ , any  $\mathbf{G}$  oriented such that

$$\left| \frac{\mathbf{G}}{\|\mathbf{G}\|} \cdot \mathbf{Y}_l \right| < \cos \theta_G \quad (11)$$

will be observed *twice* for  $\omega \in [-\pi, \pi)$ , that is, each time it intersects the cone of possible scattering vectors for its corresponding  $\theta_G$ . In the case where

$$\left| \frac{\mathbf{G}}{\|\mathbf{G}\|} \cdot \mathbf{Y}_l \right| = \cos \theta_G \quad (12)$$

it will be observed only once in the same  $\omega$ -interval, as these  $\mathbf{G}$  are tangent to the cone. The components of a reciprocal lattice vector written in the lab frame are obtained as

$$[\mathbf{G}]_l = \mathbf{R}_s^l \cdot \mathbf{R}_c^s \cdot \mathbf{B} \cdot h \begin{Bmatrix} h \\ k \\ l \end{Bmatrix} \quad (13)$$

$$= \frac{2 \sin \theta}{\lambda} \begin{Bmatrix} \cos \eta \cos \theta \\ \sin \eta \cos \theta \\ \sin \theta \end{Bmatrix}, \quad (14)$$

where the integers  $\{hkl\}$  are both the reciprocal lattice vector components as well as the Miller indices of the crystallographic plane to which  $\mathbf{G}$  is normal [25], and the angles  $\theta$ ,  $\eta$ , and  $\omega$  are measured directly from the diffraction instrument (see Fig. 1). Recall that both the detector orientation and the COM coordinates of the diffracting crystal influence the mapping of pixel coordinates on the detector to  $2\theta$  and  $\eta$ . Reciprocal lattice vectors are alternately parametrized herein by their associated Miller indices  $\{hkl\} \rightarrow \mathbf{G}_{hkl}$ , or their diffractometer angles,  $\{2\theta, \eta, \omega\} \rightarrow \mathbf{G}_{hkl}$ . By convention we choose to map the angles  $\eta$  and  $\omega$  into the interval  $[-\pi, \pi)$ ; the scattering angle  $\theta$  is restricted to the interval  $(0, \pi/2)$  by equation (8), although typical values for  $2\theta_{\max}$  in far-field HEDM are  $\leq 20^\circ$ . For a general angle  $\chi$  the mapping  $\chi \rightarrow [-\pi, \pi)$  is achieved using the expression

$$\hat{\chi} = \text{mod}\left(\frac{\chi + \pi}{2\pi}\right) - \pi \quad (15)$$

where  $\text{mod}\left(\frac{a}{b}\right)$  is the remainder of  $a/b$ , and  $\hat{\chi}$  is the mapped angle. A similar expression can be used to compute a distance measure between angles  $\chi_0$  and  $\chi_1$  insensitive to the choice of branch cut

$$\|\chi_1 - \chi_0\|_Z = \left| \text{mod}\left(\frac{(\chi_1 - \chi_0) + \pi}{2\pi}\right) - \pi \right| \quad (16)$$

Note that  $\|\cdot\|_Z$  is non-negative and in the interval  $[0, \pi]$ . This metric can be used to calculate a figure of merit for matching predicted and measured  $\mathbf{G}$  using their angular parametrizations  $\{2\theta, \eta, \omega\}$  (see

section 2.5). Equations (11), (12), and (13) can be used to calculate the number of expected reflections for a given grain (that is, embedded crystallite). To maximize the number of unique observable reflections, the strategy is to maximize  $\theta_{\max}$ , the  $\eta$ -range, and the  $\omega$ -range. Note that maximizing  $\theta_{\max}$  and the  $\theta$  (read: strain) resolution are conflicting specifications. A general rule of thumb is to choose the working distance,  $D$ , such that the effective pixel size is  $\sim 10^{-4}$ . Then x-ray energy may be tuned in the 50–100 keV range to fit the desired reflections into the range determined by  $\theta_{\max}$ . Ancillary equipment such as tensile loadframes, diamond anvil cells, or furnaces necessarily limit the achievable  $\omega$ -range, the consequences of which are examined in section 3.

### 2.2.1 Friedel pairs

The reciprocal lattice vectors  $\{hkl\} \rightarrow \mathbf{G}_{hkl}$  and  $\{\bar{h}\bar{k}\bar{l}\} \rightarrow \mathbf{G}_{\bar{h}\bar{k}\bar{l}}$  are referred to as Friedel pairs. By definition

$$\mathbf{G}_{hkl} + \mathbf{G}_{\bar{h}\bar{k}\bar{l}} = \mathbf{0} \quad (17)$$

As Friedel pairs refer to the same set of crystallographic planes in the lattice, they refer to the same interplanar spacing,  $d_G$ . They are particularly valuable in the HEDM experiment because they comprise two distinct observations of the same physical quantity.<sup>†</sup> Their role in both grain indexing, position fitting, and cell refinement are discussed in subsequent sections.

Given the angular components of an observed scattering vector,  $\{2\theta, \eta, \omega\} \rightarrow \mathbf{Q}$ , the Friedel pair to  $\mathbf{G}_{hkl} \parallel \mathbf{Q}$  can always be found as  $\{2\theta, -\eta, \omega + \pi\} \rightarrow \mathbf{G}_{\bar{h}\bar{k}\bar{l}}$ . However, for reflections satisfying equation (11) and  $\eta \neq \pm\pi/2$ ,  $\mathbf{G}_{\bar{h}\bar{k}\bar{l}}$  can also be found at  $\omega + \Delta\omega_{FP}$  where  $|\Delta\omega_{FP}| \in [2\theta, \pi)$ . Here  $\Delta\omega_{FP}$  is defined as the minimum goniometer angle required to bring the Friedel pair of  $\mathbf{G}_{hkl}$  into a Bragg condition. An expression for  $\Delta\omega_{FP}$  can be obtained by applying equations (9), (10), and (13) to  $-\mathbf{Q}$  with  $\mathbf{R}_s^l$  written in terms of  $\Delta\omega_{FP}$

$$\cos \eta \cos \theta \sin \Delta\omega_{FP} - \sin \theta \cos \Delta\omega_{FP} = \sin \theta \quad (18)$$

Equations of this form can be solved by applying the linear combination identity

$$n \sin(x) + m \cos(x) = \sqrt{n^2 + m^2} \sin(x + \text{where} = \arctan\left(\frac{m}{n}\right) + \begin{cases} 0 & \text{for } n \geq 0 \\ \pi & \text{for } n < 0 \end{cases} \quad (19)$$

<sup>†</sup>The structure factors – and thus diffracted intensities – for  $\mathbf{G}_{hkl}$  and  $\mathbf{G}_{\bar{h}\bar{k}\bar{l}}$  need not be equal for non-centrosymmetric space groups. However, equation (17) always holds.

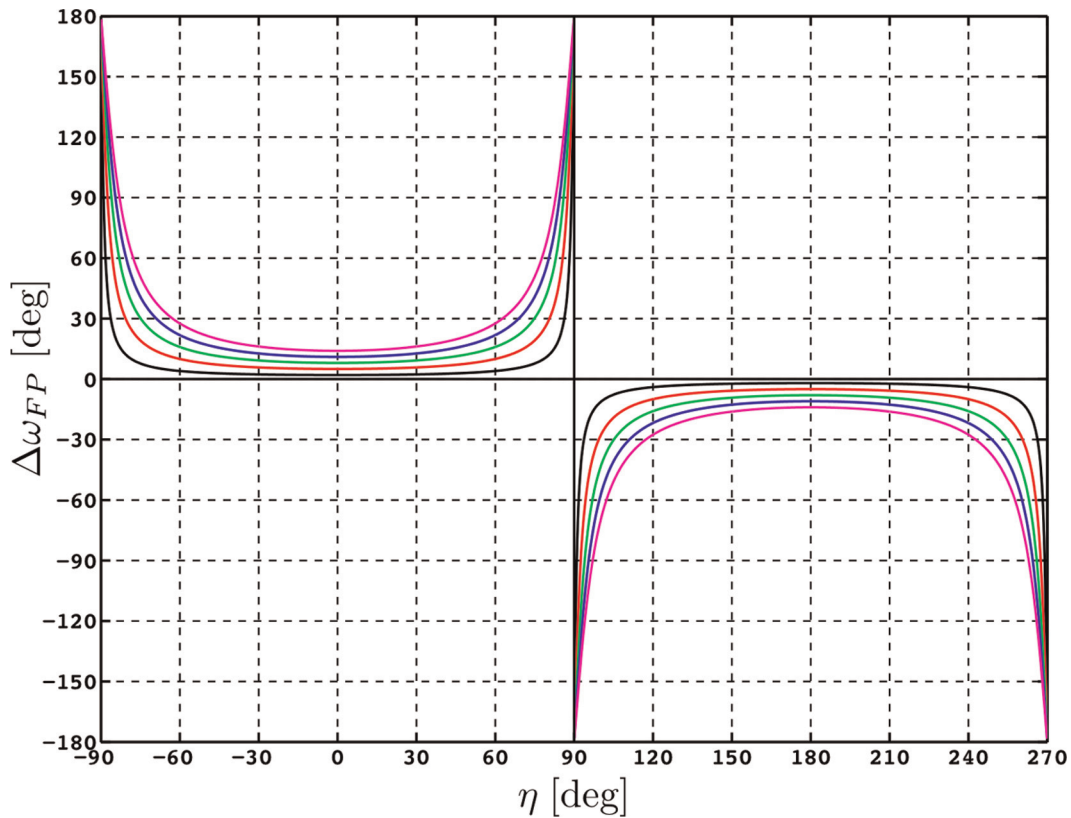


Fig. 3 Solution of equation (22) as a function of  $\eta$  for values of  $2\theta \in \{2^\circ, 5^\circ, 8^\circ, 11^\circ, 14^\circ\}$

The Friedel pairs are then parametrized as

$$\{2\theta, \eta, \omega\} \rightarrow \mathbf{G}_{hkl} \tag{20}$$

$$\{2\theta, \eta + \pi, \omega + \Delta\omega_{FP}\} \rightarrow \mathbf{G}_{\bar{h}\bar{k}\bar{l}} \tag{21}$$

Note that the case where  $n=0$  in equation (19) (that is,  $\eta = \pm\pi/2$ ), corresponds to the case described in equation (12), and  $\mathbf{G}_{hkl}$  and  $\mathbf{G}_{\bar{h}\bar{k}\bar{l}}$  are visible only once each for  $\omega \in [0, 2\pi)$ ; Fig. 3 shows  $\Delta\omega_{FP}$  as a function of  $\eta$  for several values of  $2\theta$ .

### 2.3 Detector angular calibration

The angular calibration of the detector transforms (Cartesian) pixel positions in the detector frame,  $\{\mathbf{X}_d\mathbf{Y}_d\mathbf{Z}_d\}$ , to scattering angle and azimuth,  $(2\theta, \eta)$ . Figures 1(a) and (b) illustrate the definition of these quantities with respect to the six coordinate systems described in section 2.1. It is convenient to work with components in  $\{\mathbf{X}'_d\mathbf{Y}'_d\mathbf{Z}'_d\}$  herein. The diffraction centre is denoted by  $P1'$ , the coordinates of which can change as a function of  $\omega$  if  $\mathbf{p} \neq \mathbf{0}$ . Let the change-of-basis matrix  $T$  take components from  $\{\mathbf{X}_d\mathbf{Y}_d\mathbf{Z}_d\} \rightarrow \{\mathbf{X}'_d\mathbf{Y}'_d\mathbf{Z}'_d\}$ ; this describes the effect of detector tilt (that is, non-orthogonality with respect to the incident x-ray beam). Presently, an Euler angle approach is taken to represent the tilt of the detector plane

$$T \equiv R(\gamma_z \mathbf{Z}'_d) \cdot R(\gamma_y \mathbf{Y}'_d) \cdot R(\gamma_x \mathbf{X}'_d) \tag{22}$$

where  $\gamma_x, \gamma_y, \gamma_z$  are the tilts about the  $\mathbf{X}'_d$ , rotated  $\mathbf{Y}'_d$ , and rotated  $\mathbf{Z}'_d$  axes, respectively.<sup>†</sup> The coordinates of a point on the detector provide the components of  $P4$  in  $\{\mathbf{X}_d\mathbf{Y}_d\mathbf{Z}_d\}$ . The point  $P2$  is the common origin of  $\{\mathbf{X}_d\mathbf{Y}_d\mathbf{Z}_d\}$  and  $\{\mathbf{X}'_d\mathbf{Y}'_d\mathbf{Z}'_d\}$ , and  $P2'$  is the intersection of the transmitted beam through  $P1'$  with the ideal detector plane. The point  $P3$  represents the intersection of the diffracted beam with the ideal detector plane, and can be found using (i) a parametric equation for the diffracted beam originating from  $P1'$  intersecting the detector at  $P4$ , and (ii) an equation for the ideal detector plane

$$\left. \begin{aligned} P3 &= P1' + u(P4 - P1') \\ 0 &= \mathbf{Z}'_d \cdot (P3 - P2) \end{aligned} \right\} \Rightarrow u = \frac{\mathbf{Z}'_d \cdot (P2 - P1')}{\mathbf{Z}'_d \cdot (P4 - P1')} \tag{23}$$

The scattering angle and azimuth can then be found as

$$2\theta = \cos^{-1} \left( -\mathbf{Z}'_d \cdot (\widehat{P3 - P1'}) \right) \tag{24}$$

$$\eta = \tan^{-1} \left( \frac{\mathbf{Y}'_d \cdot (P3 - P2')}{\mathbf{X}'_d \cdot (P3 - P2')} \right), \tag{25}$$

where  $(\widehat{\cdot})$  indicates a unit vector.

<sup>†</sup>This is an active rotation convention.

The reverse transformation taking  $\{2\theta, \eta, \omega\}$  to the detector-relative coordinates of  $P4$  is computed analogously to equation (23), interchanging  $P3$  and  $P4$  and using

$$P3 = (\rho \cos \eta, \rho \sin \eta, 0) + (P2' - P2) \quad (26)$$

$$\text{where } \rho = |P2' - P1'| \tan 2\theta. \quad (27)$$

It is significant to note that this geometric description is completely general and allows for arbitrary detector configurations, including cases where the beam does not intersect the detector plane.

The angles  $\{\gamma_x, \gamma_y\}$  as well as the beam centre ( $P2$ ) and working distance,  $D = |P2 - P1|$ , can be determined using a powder diffraction pattern from a standard reference material (for example, Si,  $\text{LaB}_6$ ,  $\text{CeO}_2$ ) measured at a known wavelength. Determining  $\gamma_z$  requires non-axisymmetric diffraction patterns, such as an HEDM measurement of a single crystal. Note that  $\gamma_z$  is the angle between projection of  $\mathbf{Y}_l$  and  $\mathbf{Y}_d$  (that is,  $up$  in the diffraction image).

The details of the least-squares approaches used to determine these quantities will be described elsewhere. In all cases, the objective function provides a figure of merit representing the misfit between the spatial positions of the measured and predicted diffracted beams as a function of the detector geometry.

A subtle detail not dealt with in this paper is spatial distortion in the detector. It is tacitly assumed that the measured components in  $\{\mathbf{X}_d, \mathbf{Y}_d, \mathbf{Z}_d\}$  are distortion-free. The intrinsic distortion of the GE 41RT detector used to collect the data presented in section 3.1 – as well as correction thereof – is discussed by Lee *et al.* [24]. It is significant that the spatial distortion is free of high-frequency components, contrary to what is observed in many fibre optic coupled CCD cameras. This allows for straightforward and accurate correction of the raw data. Methods for determining  $\mathbf{p}$  using a calibrated detector, or alternatively refining the beam centre coordinates ( $P2'$ ) using Friedel pairs, are described in section 2.6.2.

## 2.4 Spot finding

In the HEDM method, a 3D diffraction image is generated by exposing the detector while rotating the crystal through an interval  $\Delta\omega$  [11]. While it is desirable to minimize  $\Delta\omega$  to maximize the accuracy of the measured  $\mathbf{Q} / \mathbf{G}$  components, practical concerns regarding data volume and speed of measurement in the in situ test dictate typical values of

$\Delta\omega = 0.25^\circ - 1^\circ$ . Each image *frame* is then keyed to the mean value of  $\omega$  for each exposure ( $\dot{\omega}$  is constant). The identification of *individual* diffraction peaks in a single image – so-called *spot finding* – comprises the critical data reduction step.

The diffraction spots integrated over each  $\Delta\omega$  will exhibit intrinsic broadening along the angular directions  $\{\delta q_{2\theta}, \delta q_\eta, \delta q_\omega\}$ . These are related to (i) the intragranular strain distribution and bandwidth of the x-ray beam ( $\delta q_{2\theta}$ ); and (ii) the intragranular orientation distribution or *mosaicity* ( $\delta q_\eta$  and  $\delta q_\omega$ ). Well-annealed samples will generally have intrinsic angular widths of  $<0.1^\circ$ . Increasing dislocation content, for example, resulting from plastic deformation, can lead to spreads of several degrees or more in  $\eta$  and  $\omega$ . Beyond this limit, the spots become generally indistinguishable by segmentation methods and the patterns must be handled using forward modelling [18] or powder diffraction methods [1, 33]. The reader is directed to the work of Poulsen [34] for a comprehensive discussion of the image processing limitations of the 3DXRD/HEDM method.

Diffracted beams are identified in the 2D or 3D diffraction images by segmentation. Presently connected component labelling is employed on thresholded greyscale images. As thresholding is a somewhat heavy-handed approach to separating the useful data from noise, some care must be taken in its application. The intensities of diffracted beams from fully bathed grains will depend on several factors, including:

- the structure factor of the associated reflection;
- the associated grain volume;
- the elevation of the associated  $\mathbf{G}_{hkl}$  out of the  $\mathbf{X}_l - \mathbf{Z}_l$  plane (i.e. the Lorentz factor).

Spots may also be split between  $\omega$ -frames and require merging. Hence, differential thresholding can be employed to avoid systematically biasing against smaller grains or weaker reflections in the segmentation process.

Connected component labelling can be applied to binary images (0 below threshold, 1 above) in  $n$ -dimensions. Therefore it is possible to handle merging spots in  $\omega$  simply by segmenting the 3D image ( $\{\mathbf{X}_d, \mathbf{Y}_d, \omega\}$  or preferably  $\{2\theta, \eta, \omega\}$ ). However, this can become impractical for large image stacks. Furthermore, applying the appropriate merging logic can render sequential 2D image processing equivalent to a 3D connected component labelling. Two merging heuristics are generally applied: the stricter involves merging spots labelled on adjacent  $\omega$  frames that have *any* overlapping pixels, while the looser involves merging spots that have centroids within

a certain distance tolerance. The former is desirable for data where  $\Delta\omega$  is smaller than the intrinsic spot width,  $\delta q_\omega$ ; the latter is more appropriate for the case where  $\Delta\omega \geq \delta q_\omega$ . Potential alternatives to the connected component labelling algorithm, such as the watershed algorithm, are discussed in section 4.

Centroidal coordinates may be quickly estimated by using an intensity-weighted mean position over the full 2D or 3D bounding box containing the labelled spot. Because the intrinsic spreading of the spots in far-field HEDM data is aligned with the angular coordinates  $\{2\theta, \eta, \omega\}$  such an average could have a large error if calculated in the semi-Cartesian space  $\{\mathbf{X}_d, \mathbf{Y}_d, \omega\}$  for broad spots. Therefore it is much more accurate to perform the weighted average in the  $\{2\theta, \eta, \omega\}$  space. More accurate still is to estimate the centroid of a spot by fitting a 2D or 3D profile function. In the present implementation, 2D or 3D elliptical Gaussians are employed. Generally speaking, the defocusing associated with the far-field HEDM geometry effectively *smears* the heterogeneous intensity distributions and it is reasonable to approximate the spot shapes with symmetric profile functions. However, spot morphology may become increasingly complex – and highly asymmetric – depending on the extent of organized dislocation structures in the originating grain. One such example is the formation of dislocation cell structures in low stacking fault energy metals such as copper, as explored by Jakobsen *et al.* [35]. In the case where simple profile functions (for example, Gaussian, Lorentzian, pseudo-Voigt) do not provide satisfactory fits of the spots, then additional analysis is required. Two potential approaches include: forward-modelling techniques that uses discretization of the grain in physical and/or orientation space [18, 36]; applying a superposition of symmetric profile functions. Both topics are beyond the scope of this paper.

Various measures are taken to create a robust fitting algorithm for the spot intensity distributions. We employ numerical quadrature with the number of quadrature points per pixel in each direction chosen automatically to accurately capture any sub-pixel variation in the spot intensity. In this way, accuracy in the fitting procedure is maintained even when spot widths are only a few pixels. Pixels in the vicinity of the spot are included in the fit so that the background and tail of the distribution are well constrained.

The use of fit quality in estimating the uncertainty in the spot position, and hence  $\mathbf{Q}/\mathbf{G}$  components, has been explored in detail by Edmiston *et al.* [28]. Errors in the detector angular calibration, as well as in the accuracy and precision of the

diffractometer stages introduce bias errors in the spot positions, which is further discussed in section 4. Once the angular calibration of the detector is accurately determined, all measured data is binned by scattering angle using a tolerance  $\delta 2\theta_{hkl}$ , and thus associated with a particular family of crystallographic planes  $\{hkl\}$ . The active set of  $\{hkl\}$  is at the discretion of the user. The scattering angle tolerance need not be fixed; they are rather calculated from the Bragg law (equation (8)) using a specified tolerance on normal strains,  $\delta e_{hkl} = \Delta d_{hkl} / d_{hkl}^0$ , to account for the effects of unknown strain or errors in the reference cell parameters. The reference plane spacing,  $d_{hkl}^0$ , is calculated from the reference cell parameters and equations (6) and (13). To account for the unknown  $\mathbf{p}$ , each  $\{hkl\}$ -specific tolerance zone is padded with half of the widest beam dimension (in pixels, typically 0.5 mm) on the inner and outer radii. Reflections within the specified tolerance of more than one  $\{hkl\}$  are multiply associated until indexed. To avoid fitting noise, the images may be masked using  $\delta e_{hkl}$  on the active set of  $\{hkl\}$ . Tests including minimum spot size and maximum  $\omega$  extent can also be applied to avoid erroneously fitting *hot pixels* arising from background radiation as well as dead pixels.

## 2.5 Grain indexing

Grains are indexed from a set of trial orientations with candidates chosen among orientations satisfying a minimum completeness threshold, where completeness is defined as the ratio of observed to expected reflections for a given orientation. The methodology for choosing the set of trial orientations is critical to the efficiency of the algorithm. For each trial orientation, the complete set of expected  $\mathbf{G}_{hkl}$  corresponding to the  $\omega$ -range as well as the constraints given in equations (11) and (12) are calculated. Independent tolerances on the differences between the components of all measured  $\mathbf{Q}$  and each predicted  $\mathbf{G}_{hkl}$  must be satisfied in order for them to be associated. Alternatively, tolerances may be applied to the differences between the measured and predicted diffractometer angles  $\{2\theta, \eta, \omega\}$ . It is often simpler to assign uncertainties to the angles instead of  $\mathbf{Q}/\mathbf{G}$  components, although the angular space is more distorted. For data presented in section 3, the tolerances on the diffractometer angles  $\{2\theta, \eta, \omega\}$  were applied using the angular distance metric described by equation (20). The calculation of  $\delta 2\theta$  was discussed in the previous section. The tolerance  $\delta\omega$  depends on the azimuthal spot position accuracy, which in turn depends on the pixel size and  $2\theta$  as well as the extent and fit quality of

the spot itself. The tolerance  $\delta\omega$  depends on the oscillation step size  $\Delta\omega$  however, if  $\Delta\omega$  is small enough such that spots are split across multiple frames, and they are fit to a 3D profile function in the  $\{2\theta, \eta, \omega\}$  space, then  $\delta\omega$  can be set tighter than  $\Delta\omega$  would otherwise dictate.

Generally speaking, two options exist for generating the set of trial orientations: back-projecting the measured data, or direct discretization of orientation space. Mosciki *et al.* [17] recently introduced an indexing method based on the former approach; by contrast, the *GRAINDEX* algorithm introduced by Lauridsen *et al.* [11] and more recently the *GrainSpotter* algorithm employed by Oddershede *et al.* [9] follow the latter approach. While no one algorithm can be labelled as universally ideal for HEDM data analysis, the former approach is pursued in this paper.

Every observed diffraction spot may be associated with an orientation fibre in the orientation space

$$R(\phi) \cdot \mathbf{G} = \pm \mathbf{Q} \text{ for } \phi \in [0, 2\pi) \quad (28)$$

where  $R(\phi)$  is a one-parameter family of rotations that bring  $\mathbf{G} \parallel \pm \mathbf{Q}$ . These fibres are geodesics on  $\mathcal{SO}(3)$  [37, 38]. The  $\pm$  on the right-hand side of equation (32) reflects the centrosymmetry imparted by the diffraction [32]. If  $\mathbf{G}_{hkl}$  and  $\mathbf{G}_{\bar{h}\bar{k}\bar{l}}$  are equivalent under the crystal symmetry, then only one branch of the fibre need be considered.

The orientation of a grain is found as the *mutual intersection* of all fibres associated with its observable  $\mathbf{G}_{hkl}$ . Note, however, that subsets of fibres belonging to a grain can also intersect at other distinct points in the orientation space – a fact that effectively precludes indexing grains by searching for pair-wise fibre intersections. However, a direct search along *any* fibre associated with a grain – employing appropriate tolerances – will yield the orientation of its associated grain.

When discretizing the fibre over the angle  $\phi$ , the total number of unique points may vary from fibre to fibre under the influence of the crystal symmetry. Therefore after mapping each to the symmetrically reduced orientation space, duplicate points are removed to avoid redundancy. By using a quaternion (or any angle-axis) parametrization of the fibre, it is trivial to generate equi-spaced trial orientations of a specified misorientation.

The benefits of the fibre search approach are efficiency and robustness. In particular, robustness in terms of reliably indexing *every* complete grain in the diffraction volume, is highly desirable for the typical in situ experiment. Because the fibre search algorithm involves a series of 1D searches in orientation

space guided by the data rather than a global 3D search it is possible to gain efficiency, as described in the following paragraph. This is particularly advantageous in cases where the beam intersects the entire sample cross-section and every spot should be associated with a complete grain. In cases where the sample dimension along  $\mathbf{X}_s$  is much larger than the beam, a large fraction of spots will be associated with grains that do not remain in the beam throughout the full range of  $\omega$ ; when there are many such *incomplete* grains, particularly for very large data sets, the forward search might be more efficient.

The fibre search algorithm is greatly expedited by removing reflections from the search list once a grain containing them is indexed, which multiplicatively reduces the population of unassociated scattering vectors. In this framework, spots that are *claimed* by more than one grain can be marked as potentially overlapped spots to be handled in post-processing. This case is common in microstructures containing twin boundaries or transformed domain boundaries exhibiting a habit plane. Such conflicted spots are also removed from the completeness calculation. Completeness has been shown to be a generally robust indexing criterion over a wide range of reflection tolerances. However, there is always the possibility of erroneously assigning reflections, particularly when the lattice parameters/strain state is not well known. This can be mitigated by re-assigning reflections with tighter tolerances post refinement as the small number of erroneously assigned reflections will typically have much higher errors than the average in a given grain. If the completeness is set too low, then it is possible to mis-index grains by mis-assigning spots. However, to apply a high completeness threshold essentially requires the full refinement of the grain parameters during indexing. While this involves more computation time, it has been shown to be generally more efficient overall to properly index and remove the full set of reflections. In this scheme, the indexing algorithm provides fully refined grain objects rather than a list of orientations.

Empirical studies have indicated that for robustness – particularly for aggregates approaching ~50 000 spots and 1000 grains – a reasonable parameter set involves:

- (a) small steps along the fibre,  $\Delta\phi \sim 0.5^\circ$ ;
- (b) search fibres on 2–3 unique  $\{hkl\}$ ;
- (c) as tight a tolerance as possible on  $\eta$  and  $\omega$ ,  $\delta\eta = \delta\omega \leq \Delta\phi$ ;
- (d) a high completeness threshold, i.e.  $\geq 70$  per cent.

Employing larger steps will speed up the search, and is generally safe for small aggregates and single

crystals, but at the potential cost of robustness with respect to exhaustively searching orientation space and indexing every grain. The final ratio of assigned to unassigned  $\mathbf{Q}$  is a good indicator of whether or not a large number of grains has potentially been missed – assuming that the spot finding is relatively free of noise.

The fibre search indexing method is eminently parallelizable at the level of the individual fibre searches. Preliminary results indicate nearly ideal speedup on up to 16 simultaneous processes (see section 3.2). Parallel computing makes it feasible to employ a small fibre step size without adversely affecting the computing time. Once a candidate orientation is identified, a grain is instantiated and refined. The full refinement requires alternately refining the grain parameters and re-performing the search for measured  $\mathbf{G}_{hkl}$  at the new orientation until convergence is reached (see section 2.6). This becomes the limiting computational step in the algorithm. However, empirical studies with large aggregates – both simulated and measured – have indicated that the extra cost per grain translates into overall greater efficiency by allowing for tighter tolerances, preventing mis-indexing, and removing the maximum number of reflections from the search space as the algorithm proceeds.

It is possible to identify Friedel pairs prior to indexing (see section 2.2.1), which can be also exploited in the indexing scheme. Generally speaking, ~30–50 per cent of all observed reflections over a given  $\omega$  interval are Friedel pairs. Choosing trial orientations along the fibres associated with Friedel pairs only – particularly for high-multiplicity reflections – can significantly reduce the total number of reflections to test while still providing an exhaustive search. More attractively, however, the Friedel pairs may be used to mitigate errors in the calculated  $\{2\theta, \eta, \omega\}$  for a spot associated with the unknown centroidal coordinates of the candidate grain (see Fig. 1(b)). This can be achieved by performing the search along an averaged fibre  $\mathbf{R}(\phi) \cdot \mathbf{G}_{hkl} = \pm \mathbf{Q}$  where  $\mathbf{G}_{hkl} = (\mathbf{G}_{hkl} - \mathbf{G}_{\bar{h}\bar{k}\bar{l}})/2$ , and estimating  $p_y$ . The latter is achieved by exploiting the fact that

$$\mathbf{G}_{hkl} + \mathbf{G}_{\bar{h}\bar{k}\bar{l}} = \mathbf{0} \quad (29)$$

Note that equations (24) and (25) depend on  $\mathbf{p}$  through the coordinates of  $P1'$  and  $P2'$  and  $\omega$ . These relations can be exploited in a generalized non-linear least squares problem for  $p_y$  using the residual

$$r_{FP}(p_y) = \{ \|\theta^{(+)} - \theta^{(-)}\|_{\perp} \|\eta^{(+)} - \eta^{(-)}\|_{\perp} - \pi \} \quad (30)$$

Note that  $r_{FP} = 0$  irrespective of the absolute values of  $2\theta$  and  $\eta$ , precluding the need for highly accurate cell or orientation parameters. Unfortunately a

single Friedel pair lacks sufficient information to estimate the in-plane components of  $\mathbf{p}$  in the context of an unknown strain state (i.e. unknown  $2\theta$ ). Empirical results using the fibre search indexing algorithm are shown in section 3.

## 2.6 Distorted lattice description and refinement

Lattice or cell refinement in the context of this paper implies optimization of the parameters defining the orientation and strain of the crystal lattice after indexing. Twelve independent parameters define a crystal of a given phase in this framework: three for position, three for lattice orientation, and six for lattice distortion. The most general way of representing the linear transform that takes material vectors in the reference lattice frame to the sample frame is the affine transformation

$$\mathbf{r}' = \mathbf{F} \cdot \mathbf{r} + \mathbf{p} \quad (31)$$

where  $\mathbf{r}$  is a material vector in the fixed reference lattice and  $\mathbf{r}'$  is the material vector in the deformed configuration in the sample. This transform may be cast as a general deformation in the context of continuum mechanics, where the tensor  $\mathbf{F}$  is the deformation gradient. It is convenient to utilize the polar decomposition of  $\mathbf{F}$  which yields a pure rotation (proper orthogonal tensor) and a pure stretch (symmetric, positive-definite tensor). Thus *both* the orientation and distortion of the reference lattice in the sample frame are captured by  $\mathbf{F}$ . The polar decomposition may be ordered in one of two ways

$$\begin{aligned} \mathbf{F} &= \mathbf{R} \cdot \mathbf{U} \\ &= \mathbf{V} \cdot \mathbf{R} \end{aligned} \quad (32)$$

where  $\mathbf{R}$  is proper orthogonal,  $\mathbf{U}$  and  $\mathbf{V}$  are symmetric, positive-definite. Both decompositions are valid and give unique solutions for  $\mathbf{F}$  up to a crystal symmetry operation.

If  $\mathbf{H}^{(i)}$  is a member of the crystal symmetry group<sup>†</sup>  $\mathcal{H} \subset \mathcal{SO}(3)$ , then  $\mathbf{F}$  maps to the equivalence class

$$\mathbf{F}^* = \mathbf{F} \cdot \mathbf{H}^{(i)} \quad \forall i \in [1, N] \quad (33)$$

where  $N$  is the number of members in the symmetry group. In this context, the left polar decomposition (equation (32)) becomes a more expedient choice for representing  $\mathbf{F}$ . In the right polar decomposition,  $\mathbf{R}$  acts after the application of the stretch tensor,  $\mathbf{U}$ , which generally breaks the symmetry of the

<sup>†</sup>In the present context, this implies one of the 11 pure rotation groups.

reference lattice (the only exception being purely hydrostatic loading). In the left,  $\mathbf{R}$ , acts on the *symmetric* reference lattice and is functionally indistinguishable to the lattice orientation  $\mathbf{R}_c^s$  (see section 2.1). Because the reference lattice is physically indistinguishable in the sample frame irrespective of the choice of  $\mathbf{R} \rightarrow \mathbf{R} \cdot \mathbf{H}^{(i)}$ , the components of  $\mathbf{V}$  are unique in the sample frame. This is not the case for the components of  $\mathbf{U}$  in the crystal frame. The manifestation of the equivalence class  $\mathbf{F}^*$  is in how the signed  $(hkl)$  are assigned to the measured  $\mathbf{G}_{hkl}$ .

During indexing, the representative  $\mathbf{R} \in \mathbf{R}^*$  can be restricted to the fundamental region of orientation space associated with  $\mathcal{H}$ . This is done by generating the equivalence class for each candidate orientation and choosing the member having the minimum rotation angle. This selects a specific scheme for associating signed reciprocal lattice vector components  $(hkl)$  with the measured  $\mathbf{G}_{hkl}$ . During refinement of the cell parameters, however,  $\mathbf{R}$  is *not* restricted to the fundamental region.

The action of  $\mathbf{F}$  on the direct lattice vector components in  $\{\mathbf{X}_c \mathbf{Y}_c \mathbf{Z}_c\}$  yields the lattice vector components of the distorted cell in  $\{\mathbf{X}'_s \mathbf{Y}'_s \mathbf{Z}'_s\}$

$$\begin{aligned} \mathbf{A}' &= \mathbf{F} \cdot \mathbf{A} \\ &= [\mathbf{a}' \quad \mathbf{b}' \quad \mathbf{c}']_s \end{aligned} \quad (34)$$

The change-of-basis matrix,  $\mathbf{B}'$ , that takes components in the distorted reciprocal lattice to the sample frame is written analogously to equation (6) as

$$\mathbf{B}' = \frac{1}{v'} [\mathbf{b}' \times \mathbf{c}' \quad \mathbf{c}' \times \mathbf{a}' \quad \mathbf{a}' \times \mathbf{b}']_s \quad (35)$$

where  $v' = \mathbf{a}' \cdot \mathbf{b}' \times \mathbf{c}'$  is the distorted cell volume. With this definition, the components of  $\mathbf{G}$  for the distorted cell may be written in the lab frame as

$$\begin{aligned} [\mathbf{G}]_l &= \mathbf{R}_s^l \cdot \mathbf{B}' \cdot \begin{Bmatrix} h \\ k \\ l \end{Bmatrix} \\ &= \frac{2 \sin \theta}{\lambda} \begin{Bmatrix} \cos \eta \cos \theta \\ \sin \eta \cos \theta \\ \sin \theta \end{Bmatrix} \end{aligned} \quad (36)$$

Edmiston *et al.* [28] has shown that  $[\mathbf{G}]_l$  are equivalently obtained as

$$[\mathbf{G}]_l = \mathbf{R}_s^l \cdot \mathbf{F}^{-T} \cdot \mathbf{B} \cdot \begin{Bmatrix} h \\ k \\ l \end{Bmatrix} \quad (37)$$

Equations (36) and (37) provide the connection between the measured data and the representation

of the distorted lattice and is the basis for constructing the residual used for refining  $\mathbf{F}$  and  $\mathbf{p}$ . Note that  $\mathbf{p} \neq 0$  affects the detector angular calibration, and therefore the calculated  $\{2\theta, \eta\}$  for a spot measured on a particular  $\omega$ -frame (see Fig. 1(b)).

### 2.6.1 Lattice strain and stress tensors

The lattice strain is defined as the elastic distortion of the unit cell with respect to an *unstrained* reference lattice. As the magnitudes of such strains are typically small they are often treated as a perturbation of the reference cell. Many references applying synchrotron x-rays to strain analysis, for both powder diffraction [1, 39, 40] as well as single crystals [4, 5], take the approach of directly fitting the components of the infinitesimal strain tensor,  $\varepsilon$ , in the crystal frame. This is done using the well-known *rosette* equations

$$\begin{aligned} \frac{\Delta d}{d_0} &= \frac{\sin \theta_0}{\sin \theta} - 1 \\ &= \hat{\mathbf{G}} \cdot \varepsilon \cdot \hat{\mathbf{G}} \end{aligned} \quad (38)$$

where  $\hat{\mathbf{G}} = \mathbf{G} / \|\mathbf{G}\|$ . Equation (38) relates the change in  $d$ -spacing (via change in scattering angle) of crystallographic planes with normal  $\hat{\mathbf{G}}$  to a normal projection of. For six or more distinct reflections, a linear system may be formed on the independent components of (in 3D) and solved via least-squares methods. This approach is useful in its efficiency and generally wide scope of applicability to mechanical experiments. There are scenarios, however, when is not a suitable strain measure (for example, large elastic strains under high pressure, such as seen in diamond anvil cells).

A more general approach to strain employs finite deformation kinematics. If the full deformation gradient linking the reference lattice to the deformed lattice is known, there are many choices for strain measures. Hill [41] provided a convenient definition for a family of some particularly useful strain measures

$$\mathbf{E}_{(2m)} \equiv \begin{cases} (\mathbf{U}^{2m} - \mathbf{I}) / 2m, & m > 0 \\ \ln \mathbf{U}, & m = 0 \end{cases} \quad (39)$$

Several common strain measures obtained from equation (39) include

$$\mathbf{E}_{(0)} = \ln \mathbf{U} \quad \text{logarithmic or Hencky strain} \quad (40)$$

$$\mathbf{E}_{(1/2)} = \mathbf{U} - \mathbf{I} \quad \text{Biot strain} \quad (41)$$

$$\mathbf{E}_{(1)} = \frac{1}{2} (\mathbf{U}^2 - \mathbf{I}) \quad \text{Green - Lagrange strain} \quad (42)$$

In the small-strain limit, all of the above are equivalent. Each different strain measure is

work-conjugate to a particular stress tensor, which is beyond the scope of this paper; a suitable choice may be selected by the practitioner for the particular application. In the current implementation, the Biot strain ( $\mathbf{E}_{(1/2)}$ ) is used out of convenience.

Because the single-crystal moduli are defined in the crystal lattice, it is convenient to use crystal-relative strain measures. The current implementation solves for the components of  $\mathbf{V}$  in the sample frame ( $\{\mathbf{X}'_s \mathbf{Y}'_s \mathbf{Z}'_s\}$ ). The right stretch tensor is obtained as  $\mathbf{U} = \mathbf{R}^T \cdot \mathbf{V} \cdot \mathbf{R}$ , which will provide components in the crystal frame,  $\{\mathbf{X}_c \mathbf{Y}_c \mathbf{Z}_c\}$ . The stress tensor is then obtained as

$$\sigma = \mathbb{C} : \mathbf{E} \quad (43)$$

where  $\mathbb{C}$  is the fourth-order elastic stiffness tensor for the single crystal and the components of  $\mathbf{E}$  are calculated from  $\mathbf{U}$ .

The kinematic description presented in this section is also suitable for describing the cell distortion under non-ambient conditions, include the effects of temperature and pressure. In these cases, it is convenient to treat the stretch tensor,  $\mathbf{V}$ , as including *both* thermal and elastic effects, as diffraction does not distinguish between thermal and elastic deformations of the lattice. Thermo-elasticity models employing a single thermo-elastic stretch tensor include those based on a Grüneisen formalism [42, 43]. Because the full stretch tensor is available, both the deviatoric and hydrostatic components of the strain can be evaluated, the latter of which can be used to determine the equation of state.

### 2.6.2 Cell refinement scheme

The cell refinement for an indexed grain is achieved via an unconstrained non-linear least squares system in the 12 parameters mentioned previously. A residual is formed on the components of the measured and calculated reciprocal lattice vectors,  $\mathbf{G}_{hkl}^{(m)}$  and  $\mathbf{G}_{hkl}^{(p)}$  respectively, in the sample frame ( $\{\mathbf{X}'_s \mathbf{Y}'_s \mathbf{Z}'_s\}$ ). The exponential map parametrization [44],  $\xi = \phi \mathbf{n}$ , is used to represent the degrees of freedom in  $\mathbf{R}$ , where  $\phi$  and  $\mathbf{n}$  and  $\mathbf{n}$  are the angle and axis of the associated rotation matrix. The six independent components of the stretch tensor,  $\mathbf{V}$ , are represented in using the Mandel–Voigt parameters of the associated Biot strain tensor (see reference [9]). Operating on strain rather than stretch components is purely a numerical expedience, as their relative magnitudes are more. Explicitly stated, the optimization problem for each grain is

$$\min_{\mathbf{p}, \mathbf{F}} (f(\mathbf{p}; \xi, \mathbf{E}) = \mathbf{G}_{hkl}^{(m)}(\mathbf{p}) - \mathbf{G}_{hkl}^{(p)}(\xi, \mathbf{E})) \quad (44)$$

$\forall$  indexed  $\mathbf{G}_{hkl}$

Equations (14), (24), and (25) provide  $\mathbf{G}_{hkl}^{(m)}(\mathbf{p})$ , while equation (37) provides  $\mathbf{G}_{hkl}^{(p)}(\xi, \mathbf{E})$ . Because the optimization is restricted to the currently indexed reflections, it is prudent to search over the measured data post refinement to index any reflections that may have been omitted (i.e. outside of the specified tolerances) prior to refinement. Empirical evidence has shown that this procedure – refine, then search – generally needs to be repeated two or three times before convergence is achieved.

It is possible to solve for  $\mathbf{p}$  *independently* of the orientation and strain refinement if considering only the Friedel pairs indexed for a particular grain. This requires two or more independent Friedel pairs using the objective function given in equation (30). Recall that equation (30) works with angular differences between the measured quantities rather than absolute values. While this can be helpful during indexing, empirical studies have shown that in the presence of experimental errors it is generally better to solve for the components of  $\mathbf{p}$  simultaneously with  $\mathbf{F}$  as described above using equation (44).

Edmiston *et al.* [28] has described a framework to represent the instrumental uncertainties in  $\{2\theta, \eta, \omega\}$  as weights in the generalized least-squares formulation. This allows for the propagation of errors into  $\mathbf{p}$  and  $\mathbf{F}$ . Often the oscillation step  $\Delta\omega$  is large with respect to the uncertainties in  $2\theta$  and  $\eta$ . The available  $\omega$ -range also has a large effect on the propagation of errors to the various components of  $\mathbf{p}$  and  $\mathbf{F}$ . These are examined using simulated diffraction data in section 3.2. For a rigorous treatment of the uncertainty propagation into the degrees of freedom in  $\mathbf{F}$ , the reader is referred to the paper of Edmiston *et al.* [28].

## 3 RESULTS

### 3.1 Ruby single crystal

Six HEDM measurements were performed on a 150  $\mu\text{m}$  diameter spherical ruby single crystal (NIST SRM 1990; see reference [45]). The space group for the ruby crystal is trigonal,  $R\bar{3}c$ , with lattice parameters  $a = 4.76080 \pm 0.00029 \text{ \AA}$  and  $c = 12.99568 \pm 0.00087 \text{ \AA}$  in the hexagonal convention. A tungsten slit aperture located  $\sim 1 \text{ m}$  upstream of the sample was used to provide a  $500 \times 250 \mu\text{m}$  ( $\mathbf{X}_l \times \mathbf{Y}_l$ ) beam of 80.725 keV (0.15359  $\text{\AA}$ ) x-rays at APS beamline 1-ID-C. The range of oscillation was  $\omega \in [-60^\circ, 60^\circ]$  with  $\Delta\omega = 0.25^\circ$ , as these represent typical experimental parameters. Recall that if ancillary equipment such as a loadframe is used, the supports typically prevent the ability to use  $\omega \in [-90^\circ, 90^\circ]$  without

blocking the diffracted x-ray beams for some significant interval. A GE Revolution 41RT flat-panel detector from GE Healthcare was employed for the experiment [24, 46]. The salient features that make this detector particularly suitable for far-field HEDM include its size ( $409.6 \times 409.6$  mm) and speed of acquisition. The spatial distortion in the context of strain analysis has been well characterized. The reference pixel size is  $200 \times 200 \mu\text{m}$ . A sample of  $\text{LaB}_6$  powder (NIST SRM 660) was used for the initial angular calibration. This was further refined using a scan of the ruby standard after manually centring it in the diffractometer. The full list of geometric parameters determined by both standards are listed in Table 1.

The crystal was found to have angular spreads in  $\eta, \omega < 0.1^\circ$ . A cursory indexing was performed after locating the crystal in the x-ray beam. It was subsequently centred on the diffractometer axis by maximizing the integrated intensities of two  $\mathbf{G}_{hkl}$  as a function of the sample position in  $\{\mathbf{X}_l, \mathbf{Y}_l, \mathbf{Z}_l\}$ . This was accomplished by narrowing the beam to  $20 \mu\text{m}$  in the dimension parallel to the particular coordinate being centred; that is, the beam-defining slits were narrowed vertically to centre the grain along  $\mathbf{Y}_l$ , and horizontally to centre along  $\mathbf{X}_l$  and  $\mathbf{Z}_l$ . The  $(02\bar{2})$  reflection at  $\{2\theta, \eta, \omega\} = \{4.5^\circ, 128.0^\circ, 0.40^\circ\}$  was used to centre the crystal along  $\mathbf{X}_l$  and  $\mathbf{Y}_l$ , and the  $(208)$  reflection at  $\{6.9^\circ, -162.2^\circ, -59.1^\circ\}$  was used to centre the crystal along  $\mathbf{Z}_l$ . Because the ruby was spherical, the integrated intensities of these spots over small  $\Delta\omega$  were maximized when its centre intersected the narrowed beam, which presented the largest diffracting volume. The values of integrated intensity versus sample position over ranges large enough to move the sample completely out of the narrowed beam were fit with Gaussian functions to more precisely estimate the centre coordinate along each coordinate axis in  $\{\mathbf{X}_s, \mathbf{Y}_s, \mathbf{Z}_s\}$ .

The full  $\omega$ -scan on the centred ruby provided a baseline data set with  $\mathbf{p} = 0$ , which was also used to

**Table 1** Results of NIST SRM 1990 ruby sphere precession test. The beam centre is given relative to the lower-left hand corner of the detector. The detector is square with dimensions  $409.6 \times 409.6$  mm, containing  $2048 \times 2048$  pixels

| Parameter        | Powder fit              | Crystal fit             |
|------------------|-------------------------|-------------------------|
| $x_d$ [mm]       | 206.249                 | 206.236                 |
| $y_d$ [mm]       | 208.036                 | 208.046                 |
| $D$ [mm]         | 1050.739                | 1050.667                |
| $\gamma_x$ [deg] | $4.127 \times 10^{-2}$  | $6.904 \times 10^{-2}$  |
| $\gamma_y$ [deg] | $-1.783 \times 10^{-1}$ | $-1.587 \times 10^{-1}$ |
| $\gamma_z$ [deg] | 0                       | $-2.304 \times 10^{-2}$ |

refine the angular calibration of the detector. The positioning stages above the rotation stage were then used to manually alter  $\mathbf{p}$ , and the scans repeated. The scan speed was  $\dot{\omega} = 1.9^\circ\text{s}^{-1}$ , and the sample was rotated continuously during acquisition. This provided good integrated intensities with the strongest reflections near saturation. The image sets were masked beyond  $2\theta_{\text{max}} = 10.5^\circ$ , and around several rings where scattering from the slits interfered with the ruby spots. A relatively low threshold was used after background subtraction to minimize both the loss of low-structure factor reflections and the effects of labelling noise. Each of the six image sets contained  $\sim 1800$  labelled spots, with  $\sim 700$  unassigned to any  $\{hkl\}$  and  $\sim 400$  multiply-assigned. The unassigned spots were attributed to scattering from the downstream slit blade as well as part of a gold wire positioned near the ruby to aid in coarse alignment in the beam. Hypothetical methods for removing these extraneous spots from the segmented image data include more sophisticated masking and/or background images taken with the beam on and sample removed.

Each scan was indexed independently using the  $\{012\}$  Friedel pair in the fibre search algorithm with  $\Delta\phi = 1^\circ$ ,  $\delta e = 5 \times 10^{-3}$ , and  $\delta\eta = \delta\omega = 1^\circ$  and subsequently refined. Note that all measured  $\mathbf{G}_{hkl}$  were fit with elliptical Gaussians to determine the associated  $\{2\theta, \eta, \omega\}$  as discussed in section 2.4. After indexing,  $\sim 390$  were assigned to the ruby crystal giving an average completeness of  $\sim 85$  per cent. Inspection of the indexed data indicated that  $\mathbf{Q}$  from some low structure factor reflections were systematically absent; these were all in overlapping regions with stronger reflections, making a priori differential thresholding impossible.

The results for the input and refined  $\mathbf{p}$  for each scan are listed in Table 2. The averaged cell parameter values and mutual misorientation over the six scans are listed in Table 3. The precision and accuracy of the cell parameters is an indication of the achievable strain resolution. The deviation from the certified lattice parameters given by Wong-Ng *et al.* [45] is within  $5 \times 10^{-4}$ , however they are well within the range of from the round-robin study in the same reference. The mutual misorientation represents the average over the  $\binom{6}{2} = 15$  unique misorientations calculated over the six scans.

### 3.2 Simulated aggregate

To illustrate the performance of both the grain indexing algorithm and the grain parameter refinement, diffraction data were simulated for a large polycrystalline aggregate. The use of simulated data provides the ability to verify the robustness of the

**Table 2** Results of NIST SRM 1990 ruby sphere precession test. All dimensions in  $\mu\text{m}$ 

| Input   |       |       | Measured |       |        | Difference    |               |               |
|---|-------|-------|----------|-------|--------|---------------|---------------|---------------|
| $p_x$   | $p_y$ | $p_z$ | $p_x$    | $p_y$ | $p_z$  | $p_x$         | $p_y$         | $p_z$         |
| 0   | 0     | 0     | 1.5      | -0.1  | -2.0   | 1.5           | -0.1          | -2.0          |
| -100  | 50    | -100  | -101.8   | 51.0  | -105.6 | -1.8          | 1.0           | -5.6          |
| -100  | 50    | 100   | -101.5   | 50.9  | 94.3   | -1.5          | 0.9           | -5.7          |
| -150  | -50   | 0     | -151.7   | -53.9 | -7.3   | -1.7          | -3.9          | -7.3          |
| -50   | 10    | -50   | -49.3    | 10.6  | -54.4  | 0.7           | 0.6           | -4.4          |
| -25   | 5     | -25   | -23.0    | 6.6   | -27.7  | 2.0           | 1.6           | -2.7          |
| <b>Mean Error Magnitude <math>\pm</math> std. dev</b> |       |       |          |       |        | $1.5 \pm 0.4$ | $1.4 \pm 1.2$ | $4.6 \pm 1.8$ |

**Table 3** Cell refinement results from NIST SRM 1990 ruby sphere precession test. Lattice parameters  $\{a, b, c\}$  are in  $\text{\AA}$ , and all angles are in degrees

|   | Cell Parameters             |                            |                              |
|---|-----------------------------|----------------------------|------------------------------|
|   | $a$                         | $b$                        | $c$                          |
| <b>Round-robin [45]</b>   | $4.7608 \pm 0.0062$         | $4.7609 \pm 0.0057$        | $12.9979 \pm 0.0200$         |
| <b>Precession Measurements</b>  | $4.7610 \pm 0.0003$         | $4.7602 \pm 0.0003$        | $12.9890 \pm 0.0007$         |
|   | $\alpha = 89.993 \pm 0.002$ | $\beta = 90.023 \pm 0.004$ | $\gamma = 119.980 \pm 0.001$ |
| <b>Ensemble Misorientation</b><br>$\angle_{ij}$ for $ij \in \binom{6}{2}$ , 15 combinations | $0.003 \pm 0.001$           |                            |                              |

indexing scheme as well as examine the effects of errors in the measured  $\{2\theta, \eta, \omega\}$  and restrictions on the  $\omega$ -range in a systematic manner. This is by no means an exhaustive test of the indexing and refinement methods. Errors introduced during the image segmentation (section 2.4), including omitted and overlapped spots, are not considered here. Indeed, a comparative study of various segmentation, indexing, and refinement methods merits future study. The present focus is restricted to the effects of  $\omega$ -range and typical uncertainties in the complete list of  $\{2\theta, \eta, \omega\} \rightarrow \mathbf{G}_{hkl}$  on the determination of  $\mathbf{p}$  and  $\mathbf{F}$ .

For this study an aggregate of 819 grains was created with COM coordinates on a  $13 \times 7 \times 9$  regular grid spanning  $1 \times 0.5 \times 0.6$  mm and initially centred in  $\{X_i Y_i Z_i\}$ . The reference lattice and diffraction volume dimensions were chosen to mimic the Ti-7%Al (space group  $P6/mmc$ ,  $a = 2.925 \text{\AA}$ ,  $c = 4.674 \text{\AA}$ ) examined in the recent work of Lienert *et al.* [7]. The grain orientations and strain states were randomly assigned. Strain components were chosen from a scaled normal distribution with a mean perturbation magnitude of  $1 \times 10^3$ , which is moderately large for most metals under ambient conditions. From the simulated  $\mathbf{p}$  and  $\mathbf{F}$ , the full set of observable  $\{2\theta, \eta, \omega\}$  was generated using the detector geometry measured for the experiment described in reference [6] and  $\omega \in [-90^\circ, 90^\circ]$ . The full parameter set (listed in Table 4) represent typical values for a far-field HEDM experiment. The full data consisted of 65432 reflections over nine distinct  $\{hkl\}$ . The

strain based tolerance was  $1 \times 10^2$ , which leads to 20143 multiply-assigned spots. To assess the impact of experimental noise, the diffractometer angles  $\{2\theta, \eta, \omega\}$  were perturbed with white noise. The mean magnitudes were set to match the mean errors between predicted and measured  $\{2\theta, \eta, \omega\}$  from the ruby scans:  $u_{2\theta} = 0.0011^\circ$ ,  $u_\eta = 0.011^\circ$ ,  $u_\omega = 0.023^\circ$ . These are taken as realistic, if not somewhat idealized, uncertainty magnitudes for isolated spot positions in a typical HEDM experiment.

Three cases were analysed: one using the full  $\omega$ -range, another using  $\omega \in [-60^\circ, 60^\circ]$ , and a third using  $\omega \in [-30^\circ, 30^\circ]$ . In each case, the fibre search algorithm was run over the  $\{100\}$ ,  $\{002\}$ ,  $\{110\}$  fibres using  $\delta\phi = 0.5^\circ$ ,  $\delta\eta = \delta\omega = \delta\phi$ , and a completeness threshold of 70%. The search was not restricted to Friedel pairs only. All grains were successfully indexed from the

**Table 4** Detector parameters used for the generating the synthetic aggregate data. These parameters were measured from a  $\text{CeO}_2$  powder pattern at 80.725 keV for the experiment described in reference [6]

| Parameter        | Powder fit          |
|------------------|---------------------|
| $x_d$ [mm]       | 206.252             |
| $y_d$ [mm]       | 208.041             |
| $D$ [mm]         | 1788.932            |
| $\gamma_x$ [deg] | $8.842 \times 10^2$ |
| $\gamma_y$ [deg] | $1.864 \times 10^1$ |
| $\gamma_z$ [deg] | 0                   |

synthetic  $\{2\theta, \eta, \omega\}$  data in each case. The scalability results of the fibre search algorithm on an SMP parallel architecture for the full  $\omega$ -range are shown in Fig. 4.

Following the indexing, the grain list was sequentially refined using tighter angular tolerances ( $\delta\eta = 0.125^\circ$ ,  $\delta\omega = 0.25^\circ$ ). The full grain parameter refinement and subsequent  $\mathbf{G}_{hkl}$  assignment search was repeated for each grain until the change in the objective function value was  $< 1 \times 10^{-6}$ ; the median number of iterations was three. Errors were then calculated from the resulting fits for each grain's  $\mathbf{p}$ ,  $\mathbf{R}$ , and  $\mathbf{V}$  with respect to their known reference values. The results are plotted as histograms in

Figs 5, 6, and 7. Note that the errors in  $\mathbf{p}$  and  $\mathbf{F}$  drop to the order of machine precision when the superposition of noise to the  $\{2\theta, \eta, \omega\}$  coordinates is omitted, which indicates both self-consistency and well-posedness of the optimization problem.

#### 4 DISCUSSION

The results for  $\mathbf{p}$  from the ruby crystal are very encouraging, considering the large pixel size of the detector ( $200 \mu\text{m}$ ) and small angular spread of the sample. They indicate a mean component accuracy of  $\sim 0.025$  pixels. Considering that the sample is

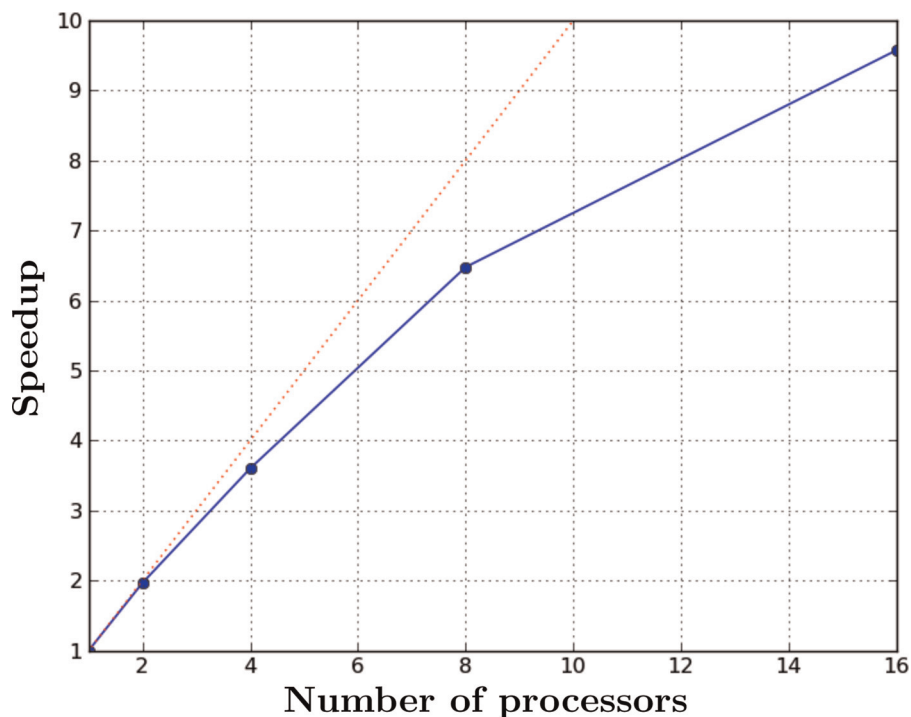


**Fig. 4** Speedup of the parallel fiber search as a function of number of processors. Speedup is calculated as the ratio of wall clock time with 1 process versus  $N$  processes on the SMP architecture. Ideal speedup is indicated by the dashed line

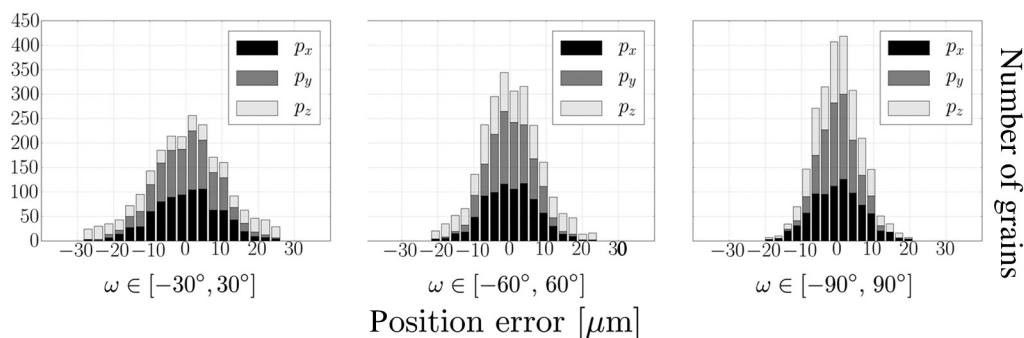


**Fig. 5** Stacked histograms of COM coordinate errors calculated from the simulated data for the indicated  $\omega$ -ranges. All components are written in the lab frame,  $\mathbf{X}_i$ , in units of  $\mu\text{m}$

never rotated such that  $\mathbf{Z}_s$  is perpendicular to the beam ( $\omega = 90^\circ$ ), it is not surprising that the relative error in  $p_z$  is larger than for  $p_x$  and  $p_y$ . This result is corroborated by the analysis of the simulated aggregate data. Given the rather small spread of individual spots in detector pixels (4–5 FWHM), this level of accuracy appears surprising. However, sufficiently accurate fits of the individual diffraction peaks were obtained using the adaptive quadrature discussed in section 2.4 to achieve this level of accuracy in the ensemble fits for  $\mathbf{p}$  and  $\mathbf{F}$  via equation (44). Because the effect of  $\mathbf{p}$  on the components of all indexed  $\mathbf{G}_{hkl}^{(m)}$  for a grain is strictly a function of  $\omega$ , accuracy is limited by  $\Delta\omega$ . While it is desirable to minimize  $\Delta\omega$  to maximize accuracy, these results indicate that choosing  $\Delta\omega \sim \delta\omega, \delta\eta$  can provide sufficient data for fitting distributions to the diffraction spots with sub-pixel resolution.

Another salient result is the precision of both the strain (deviation from reference lattice parameters) and orientation components of  $\mathbf{F}$  across the six measurements, particularly considering the rather large displacement imposed between the different tests. This has very positive implications for tracking of evolving deformations during an in situ experiment. While the measured lattice parameters presented in Table 3 differ by between 1 percent and 6 percent from the certified parameters given by Wong-Ng *et al.* [45], they are well within the range of measured values from the round-robin study documented in the same paper.

The results from the simulated data offer insight into the influence errors in  $\mathbf{p}$  have on the strain. The addition of white noise to the simulated  $\mathbf{G}_{hkl}$  was motivated by the errors observed in the ruby experiment, which itself represents something of a *best case*. A more detailed analysis of the effects of increasing errors in each of the angular coordinate was not undertaken here, but is certainly worthy of future study. Rather, we focused on gleaning the more qualitative effects on  $\mathbf{p}$  and  $\mathbf{F}$  associated with a restricted  $\omega$ -range in the presence of typical experimental errors.

This is pertinent to the design of ancillary equipment for in situ experiments, such as diamond anvil cells, where restrictions in the  $\omega$ -range are unavoidable.

It bears noting that the total number of reflections for a typical grain in the simulation is  $N \approx 80$ , which is much less than for the ruby. Restricting the  $\omega$ -range further reduces  $N$ , which affects the observed errors propagated to  $\mathbf{p}$  and  $\mathbf{F}$ . In an idealized sense, the error magnitudes scale as  $1/\sqrt{N}$ . Errors introduced via the image segmentation, such as omitted and overlapped spots, are not considered in this study. Intensity variations due to both structure factor and grain size distribution can conspire to cause systematic omissions in measured data, particularly for small grains. Restricting the  $\omega$ -range, however, represents a severe systematic omission that has a much larger effect than randomly omitting the same number of spots.

As the  $\omega$ -range is restricted from  $[-90^\circ, 90^\circ]$ , where every  $\mathbf{G}_{hkl}$  satisfying equation (11) or 12 is observed at least once, the mean error magnitudes error increase unilaterally for  $\mathbf{p}$ ,  $\mathbf{R}$ , and  $\mathbf{V}$ . In relative terms, the orientation errors are least affected, with the mean increasing from  $\sim 0.005^\circ$  to  $\sim 0.01^\circ$  over the three trials (see Fig. 6). There is also little difference between the results from the  $120^\circ$  range as compared to the full  $180^\circ$  range. These results indicate that the rotation, or orientation, is relatively well-determined in far-field HEDM even for restricted oscillation ranges. The largest discrepancies are found in the  $\mathbf{p}$  and  $\mathbf{V}$ , which both change dramatically with decreasing  $\omega$ -range.

For the  $60^\circ$  range, the errors in  $p_z$ , shown in Fig. 5, are quite large and widely distributed. The errors tighten considerably with increasing angular range, with those for the in-plane components  $p_x, p_z$  becoming equally distributed for the full range. The errors in  $p_y$  are consistently smaller because its calculation for a given grain does not depend on the  $\omega$  coordinates; it is only sensitive to the errors in  $2\theta$  and  $\eta$ . The relative standard deviations for the

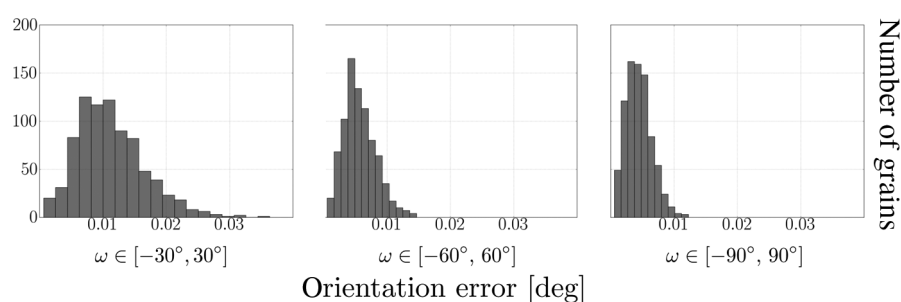


**Fig. 6** Histograms of orientation errors calculated from the simulated data for the indicated  $\omega$ -ranges. These are the magnitude (angle) of the associated misorientations, and the units are degrees

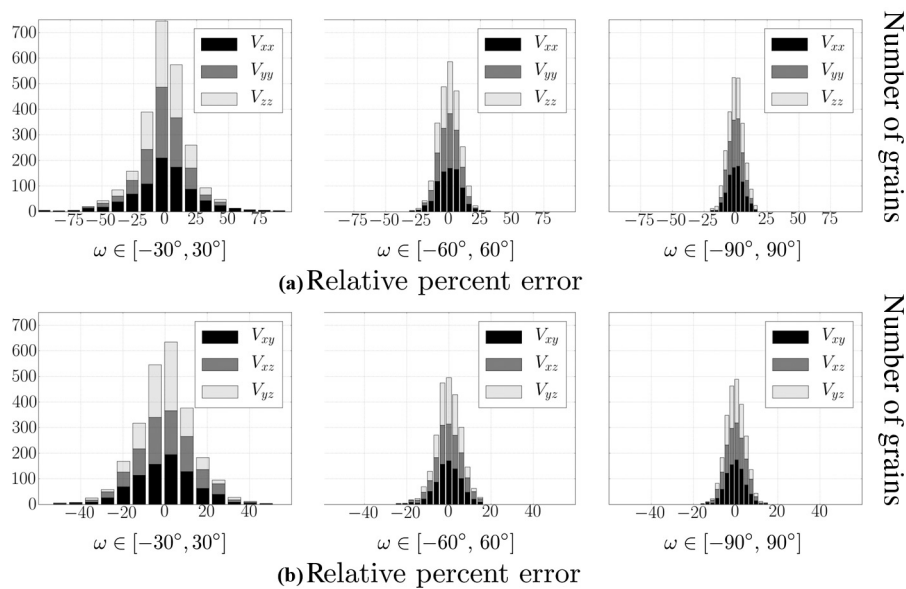


**Fig. 7** Stacked histograms of relative per cent errors in the fit stretch tensors,  $\mathbf{V}$ , calculated from the simulated data for the indicated  $\omega$ -ranges. (a) shows the normal components and (b) shows the shear components. All components are written in the sample frame,  $\mathbf{X}_s$ . The normalization factor is the input mean strain magnitude,  $1 \times 10^3$

errors in  $p_x[\mu\text{m}]/p_y[\mu\text{m}]$  for each  $\omega$ -range are 9.0/8.5 ( $\pm 30^\circ$ ), 7.2/5.9 ( $\pm 60^\circ$ ), and 6.8/4.8 ( $\pm 90^\circ$ ).

When the rotation of the sample is severely restricted and  $\mathbf{Z}'_s$  remains close to the  $\mathbf{Z}_b$ , the errors in  $p_z$  effectively corrupt the *measured*  $2\theta$  values more so than  $\eta$ . This is readily apparent in the errors in the stretch tensor components shown in Fig. 7. Upon first examination, it may appear counter-intuitive that the errors in  $V_{xx}$  are slightly larger and more widely distributed than those for  $V_{zz}$ . However, this is precisely due to the large  $2\theta$  errors imparted by the large errors in  $p_z$ . The majority of the data have largest projections onto  $\mathbf{X}'_s$ , but the errors in the observed strain (read:  $2\theta$ ) are also largest when  $\omega$  is near 0. The shears in the sample frame are more isotropically affected in each case. This may be attributed to the fact that they are most strongly influenced by the inter-planar angles, and hence the relative  $\eta$  and  $\omega$  values measured for each  $\mathbf{G}_{hkl}$ .

It is interesting and encouraging that the errors in centroid, orientation, and strain are only marginally larger for the  $120^\circ$  range as compared to those for the full range. These results indicate that maximizing the  $\omega$ -range is paramount to accuracy in the far-field HEDM method. The potential gains afforded by smaller effective pixel size, smaller x-ray bandwidth, and more precise positioning stages pale in comparison. Nevertheless, future studies examining more rigorously the limits in accuracy as a function of these higher-order parameters are warranted.

Regarding indexing methods, particularly in terms of the trade-offs between robustness and speed, it will

be advantageous to have a suite of algorithms available. It is almost a certainty that different algorithms will perform better for particular sizes of the aggregates, the volume of reciprocal space interrogated, and the needs of the experiment (for example, is it necessary to find few *special* grains to track or to maximize statistics?). The fibre search method presented in this paper has been shown to be robust, and to scale quite well using parallel computing (see Fig. 4). The scope of applicability presupposes, however, that the data consists of distinguishable spots whose centroids are determinable to relatively high accuracy.

As this experimental technique matures and more researchers develop the requisite analysis methods and software, it will become increasingly important to compare methods and identify the limitations, perhaps via round-robin samples and/or simulated data, to both grow the user community and advance the technique.

Towards these ends, an ongoing effort rooted in the analysis presented here is the development of open-source software package for HEDM data analysis. This includes interfaces for detector calibration, image processing, indexing, and grain refinement. Special capabilities include tools for identifying twins and phase transformation variants.

This technique has potential to advance many fields of study in materials science by providing high-fidelity, 3D data at the grain scale. The arena of applications encompass a wide range of problems, including (but not limited to) residual stress, anisotropic elastic moduli determination, determination of strength on a mechanistic basis (for

example, slip, twinning, phase transformations), and recrystallization/grain growth. Efstathiou *et al.* [47] have recently integrated HEDM data with finite element-based simulations to create a framework for determining single-crystal elastic moduli, presenting an application to a  $\beta$ -Titanium alloy. Another application of far-field HEDM with potentially significant impact is high-pressure research employing diamond anvil cells. The ability to identify the orientation and strain state of new phase/twin domains as they form in situ could illuminate phase transformation mechanisms [48] and produce high-fidelity equation of state and strength measurements [49].

## 5 SUMMARY

A methodology for applying the rotating crystal method to high-energy synchrotron x-ray diffraction is presented. Using far-field HEDM, it is possible to determine the orientations, centre-of-mass coordinates, and strain tensors for up to  $\sim 1000$  embedded grains in a polycrystal to a high degree of precision. A robust, parallel indexing algorithm is also presented that uses the geometry of Friedel pairs and orientation fibres to generate candidate orientations. Lastly, a continuum mechanics based framework is introduced to describe an arbitrarily oriented and distorted crystal with respect to a strain-free reference lattice. All data and software used to generate the results in this paper can be provided upon request.

## ACKNOWLEDGEMENTS

We thank Søren Schmidt, Henning Friis Poulsen, Jette Oddershede, Jon Wright, and Donald Boyce for their input and many helpful discussions during the course of this research. Use of the Advanced Photon Source was operated by UChicago Argonne, LLC, for the U.S. Department of Energy, under Contract No. DEAC02-06CH11357. This work performed under the auspices of the U.S. Department of Energy by Lawrence Livermore National Laboratory under Contract DE-AC52-07NA27344 (LLNL-JRNL-466499).

## FUNDING

Bernier and Barton gratefully acknowledge funding under the Laboratory Directed Research and Development program (LDRD 10-ERD-053). Miller acknowledges funding for this work provided by the ONR/DARPA D 3D programme (Dr Julie Christodoulou programme director) under Grant No. N00014-05-1-0505.

© Authors 2011

## REFERENCES

- 1 **Bernier, J. V. and Miller, M. P.** A direct method for the determination of the mean orientation-dependent elastic strains and stresses in polycrystalline materials from strain pole figures. *J. Appl. Crystallogr.*, 2006, **39**(3), 358–368.
- 2 **Bernier, J. V., Miller, M. P., Park, J. S., and Lienert, U.** Quantitative stress analysis of recrystallized ofhc cu subject to deformation *in situ*. *J. Engng Mater. Technol.*, 2008a, **130**(2), 021021.
- 3 **Bernier, J. V., Park, J. S., Pilchak, A. L., Glavicic, M. G., and Miller, M. P.** Measuring stress distributions in ti-6al-4v using synchrotron x-ray diffraction. *Metall. Mater. Trans. A*, 2008b, **39**(13), 3120–3133.
- 4 **Margulies, L., Lorentzen, T., Poulsen, H. F., and Leffers, T.** Strain tensor development in a single grain in the bulk of a polycrystal under load. *Acta Mater.*, 2002, **50**(7), 1771–1779.
- 5 **Martins, R. V., Margulies, L., Schmidt, S., Poulsen, H. F., and Leffers, T.** Simultaneous measurement of the strain tensor of 10 individual grains embedded in an all tensile sample. *Mater. Sci. Engng A*, 2004, **387–389**, 84–88.
- 6 **Aydner, C. C., Bernier, J. V., Clausen, B., Lienert, U., Tomé, C. N., and Brown, D. W.** Evolution of stress in individual grains and twins in a magnesium alloy aggregate. *Phys. Rev. B*, 2009, **80**(2), 024113(6).
- 7 **Lienert, U., Brandes, M. C., Bernier, J. V., Weiss, J., Shastri, S. D., Mills, M. J., and Miller, M. P.** In-situ single grain peak profile measurements on ti-7al during tensile deformation. *Mater. Sci. Engng A*, 2009, **524**, 46–54.
- 8 **Hedström, P., Han, T. S., Lienert, U., Almer, J., and Odén, M.** Load partitioning between single bulk grains in a two-phase phase duplex stainless steel during tensile loading. *Acta Mater.*, 2010, **5**, 734–744.
- 9 **Oddershede, J., Schmidt, S., Poulsen, H. F., Sørensen, H. O., Wright, J., and Reimers, W.** Determining grain resolved stresses in polycrystalline materials using three-dimensional x-ray diffraction. *J. Appl. Crystallogr.*, 2010, **43**(3), 539–549.
- 10 **Poulsen, H. F., Nielsen, S. F., Lauridsen, E. M., Schmidt, S., Suter, R. M., Lienert, U., Margulies, L., Lorentzen, T., and Jensen, D. Juul** Three-dimensional maps of grain boundaries and the stress state of individual grains in polycrystals and powders. *J. Appl. Crystallogr.*, 2001, **34**(6), 751–756.
- 11 **Lauridsen, E. M., Schmidt, S., Suter, R. M., and Poulsen, H. F.** Tracking: a method for structural characterization of grains in powders or polycrystals. *J. Appl. Crystallogr.*, 2001, **34**, 744–750.
- 12 **Larson, B. C., Yang, Wenge, Ice, G. E., Budai, J. D., and Tischler, J. Z.** Three-dimensional x-ray structural microscopy with submicrometre resolution. *Nature*, 2002, **415**, 887–890.
- 13 **Tamura, N., Spolenak, R., Valek, B. C., MacDowell, A. A., Padmore, H. A., and Patel, J. R.**

- Submicron x-ray diffraction and its applications to problems in materials and environmental science. *Rev. Sci. Instrum.*, 2002, **73**, 1369–1372.
- 14 Rogan, R. C., Tamura, N., Swift, G. A., and Üstündag, E. Direct measurement of triaxial strain fields around ferroelectric domains using x-ray microdiffraction. *Nature Mater.*, 2003, **2**, 379–381.
  - 15 Ice, G. E., Larson, B. C., Tischler, J. Z., Liu, W., and Yang, W. X-ray microbeam measurements of subgrain stress distributions in polycrystalline materials. *Mater. Sci. Engng A*, 2005, **399**, 43–48.
  - 16 Larson, B. C., Tischler, J. Z., El-Azab, A., and Liu, W. Dislocation density tensor characterization of deformation using 3d x-ray microscopy. *J. Engng Mater. Technol.*, 2008, **130**, 021024–1–10.
  - 17 Mosciki, M., Kenesei, P., Wright, J., Pinto, H., Lippman, T., Borbély, A., and Pyzalla, A. R. Friedel-pair based indexing method for characterization of single grains with hard x-rays. *Mater. Sci. Engng A*, 2009, **524**, 64–68.
  - 18 Suter, R. M., Hennessy, D., Xiao, C., and Lienert, U. Forward modeling method for microstructure reconstruction using x-ray diffraction microscopy: Single-crystal verification. *Rev. Sci. Instrum.*, 2006, **77**, 123905.
  - 19 Suter, R. M., Hefferan, C., Li, S. F., Hennessy, D., Xiao, C., Lienert, U., and Tieman, B. Probing microstructure dynamics with x-ray diffraction microscopy. *J. Engng Mater. Technol.*, 2008, **130**, 021007.
  - 20 Ludwig, W., Reischig, P., King, A., Herbig, M., Lauridsen, E. M., Johnson, G., Marrow, T. J., and Buffière, J. Y. Three-dimensional grain mapping by x-ray diffraction contrast tomography and the use of friedel pairs in diffraction data analysis. *Rev. Sci. Instrum.*, 2009, **80**(3), 033905.
  - 21 Schmidt, S., Olsen, U. L., Poulsen, H. F., Sørensen, H. O., Lauridsen, E. M., Margulies, L., Maurice, C., and Jensen, D. Juul Direct observation of 3D grain growth in Al-0.1% mn. *Scr. Mater.*, 2008, **59**, 491–494.
  - 22 Harland, C. J., Akhter, P., and Venables, J. A. Accurate microcrystallography at high spatial resolution using electron back-scattering patterns in a field emission gun scanning electron microscope. *J. Phys. E: Sci. Instrum.*, 1981, **14**(2), 175–182.
  - 23 Wright, Stuart I., Adams, Brent L., and Kunze, Karsten Application of a new automatic lattice orientation measurement technique to polycrystalline aluminum. *Mater. Sci. Engng A*, 1993, **A160**(2), 229–240.
  - 24 Lee, John H., Aydner, C. Can, Almer, Jonathan, Bernier, Joel, Chapman, Karena W., Chupas, Peter J., Haeflner, Dean, Kump, Ken, Lee, Peter L., Lienert, U., Miceli, A., and Vera, G. Synchrotron applications of an amorphous silicon flat-panel detector. *J. Synchr. Radiat.*, 2008a, **15**(5), 477–488.
  - 25 Cullity, B. D. *Elements of x-ray diffraction*, 2nd edition, 1978, pp. 480–496 (Addison-Wesley, New York).
  - 26 Warren, B. E. *X-ray diffraction*, 1990 (Dover Publications, New York).
  - 27 Withers, Philip J., Daymond, Mark R., and Johnson, Michael W. The precision of diffraction peak location. *J. Appl. Crystallogr.*, 2001, **34**(6), 737–743.
  - 28 Edmiston, J. K., Barton, N. R., Bernier, J. V., Johnson, G. C., and Steigmann, D. J. Precision of lattice strain and orientation measurements using high energy monochromatic x-ray diffraction. *J. Appl. Crystallogr.*, 2011, **44**, 299–312.
  - 29 Nye, J. F. *Physical properties of crystals: their representation by tensors and matrices*, Appendix B, pp. 276–288, 1985 (Oxford University Press).
  - 30 Neustadt, R. J., Cagle Jnr, F. W., and Waser, J. Vector algebra and the relations between direct and reciprocal lattice quantities. *Acta Crystallogr. A*, 1968, **24**(1), 247–248.
  - 31 Als-Nielsen, J. and McMorrow, D. *Elements of modern x-ray physics*, 2000 (Wiley, New York).
  - 32 Kocks, U. F. Anisotropy and symmetry. In *Texture and anisotropy: preferred orientations in polycrystals and their effects on materials properties* (Eds U. F. Kocks, C. N. Tomé, and H. R. Wenk), 2001, chapter 1, pp. 10–43 (Cambridge University Press).
  - 33 Bernier, Joel V., Miller, Matthew P., and Boyce, Donald E. A novel optimization-based pole-figure inversion method: comparison with WIMV and maximum entropy methods. *J. Appl. Cryst.*, 2006, **39**(5), 697–713.
  - 34 Poulsen, H. F. *Three dimensional x-ray diffraction microscopy*, Springer Tracts in Modern Physics, Vol. 205, 2004 (Springer, Berlin).
  - 35 Jakobsen, B., Poulsen, H. F., Lienert, U., Almer, J., Shastri, S. D., Sørensen, H. O., Grundlach, C., and Pantleon, W. Formation and subdivision of deformation structures during plastic deformation. *Science*, 2006, **312**, 889–892.
  - 36 Hansen, P. C., Sørensen, H. O., Sukosd, Z., and Poulsen, H. F. Reconstruction of single-grain orientation distribution functions for crystalline materials. *SIAM J. Imaging Sci.*, 2009, **2**(2), 593–613.
  - 37 Morawiec, A. and Field, D. P. Rodrigues parameterization for orientation and misorientation distributions. *Phil. Mag. A*, 1996, **73**(4), 1113–1130.
  - 38 Barton, N. R., Boyce, D. E., and Dawson, P. R. Pole figure inversion using finite elements over Rodrigues space. *Text. Microstruct.*, 2002, **35**(2), 113–144.
  - 39 Korsunsky, Alexander M., Wells, Karen E., and Withers, Philip J. Mapping two-dimensional state of strain using synchrotron x-ray diffraction. *Scr. Mater.*, 1998, **39**(12), 1705–1712.
  - 40 Wanner, A. and Dunand, D. Synchrotron x-ray study of bulk lattice strains in externally loaded cumo composites. *Metall. Mater. Trans. A*, 2000, **31**(11), 2949–2962.
  - 41 Hill, R. On constitutive inequalities for simple materials – I. *J. Mech. Phys. Solids*, 1968, **16**, 229–242.
  - 42 Becker, R. Effects of crystal plasticity on materials loaded at high pressures and strain rates. *Int. J. Plasticity*, 2004, **20**(11), 1983–2006.
  - 43 Barton, Nathan R., Winter, Nicholas W., and Reaugh, John E. Defect evolution and pore

- collapse in crystalline energetic materials. *Modeling Simul. Mater. Sci. Engng.*, 2009, **17**, 035003.
- 44 **Kumar, A.** and **Dawson, P. R.** Modeling crystallographic texture evolution with finite elements over neo-Eulerian orientation spaces. *Comput. Methods Appl. Mech. Engng.*, 1998, **153**, 259–302.
- 45 **Wong-Ng, W., Siegrist, T., DeTitta, G. T., Finger, L. W., Evans Jr, H. T., Gabe, E. J., Enright, G. D., Armstrong, J. T., Levenson, M., Cook, L. P., and Hubbard, C. R.** Standard reference material (SRM 1990) for single crystal diffractometer alignment. *J. Res. Natl Inst. Stand. Technol.*, 2001, **106**(6), 1071–1095.
- 46 **Lee, J. H., Aydiner, C. C., Almer, J., Bernier, J. V., Chapman, K. W., Chupas, P. J., Haeffner, D., Kump, K., Lee, P. L., Lienert, U., Miceli, A., and Vera, G.** Synchrotron applications of an amorphous silicon flat-panel detector. *J. Synchrotron Rad.*, 2008b, **15**(5), 477–488.
- 47 **Efstathiou, C., Boyce, D. E., Park, J. S., Lienert, U., Dawson, P. R., and Miller, M. P.** A method for measuring single-crystal elastic moduli using high-energy x-ray diffraction and a crystal-based finite element model. *Acta Mater.*, 2010, **58**, 5806–5819.
- 48 **Merkel, S., Wenk, H. R., Gillet, P., Mao, H. K., and Hemly, R. J.** Deformation of polycrystalline iron up to 30 GPA and 1000 K. *Phys. Earth Planet. Inter.*, 2004, **145**, 239–251.
- 49 **Dewaele, A. and Loubeyre, P.** Mechanical properties of tantalum under high pressure. *Phys. Rev. B*, 2005, **72**(13), 134106.